AIAA JOURNAL
Vol. 45, No. 11, November 2007

Large-Eddy Simulation of Separation Control for Flow over a Wall-Mounted Hump

Philip E. Morgan,* Donald P. Rizzetta,† and Miguel R. Visbal‡
U.S. Air Force Research Laboratory,
Wright–Patterson Air Force Base, Ohio 45433-7512

DOI: 10.2514/1.22660

This work describes an implicit large-eddy simulation for active control of flow over a wall-mounted hump. Results are presented for the baseline simulation without flow control and for both steady-suction and oscillatory blowing-and-suction flow control. Results are compared with Reynolds-averaged Navier–Stokes solutions and experimental data from NASA's 2004 Computational Fluid Dynamics Validation on Synthetic Jets and Turbulent Separation Control Workshop. The baseline and steady-suction cases achieved significantly better agreement with experimental flowfield characteristics than the Reynolds-averaged Navier–Stokes simulations in the separated region downstream of the hump. Because the large-eddy simulation was accomplished at one-fifth of the experimental Reynolds number, the oscillatory flow control displayed less effectiveness than the experiment. Using a larger oscillatory amplitude exerts more control on the separation bubble. Comparing the baseline flow solution with cases using flow control clearly demonstrates the ability to reduce the size of the separated flow region in the wake of the hump.

Nomenclature

M_∞	=	Mach number
Pr	=	Prandtl number, 0.73 for air
Re_c	=	reference Reynolds number, $\rho_\infty u_\infty c/\mu_\infty$
U, V, W	=	contravariant velocity components
x, y, z	=	nondimensional Cartesian coordinates in the streamwise, vertical, and spanwise directions
γ	=	specific heat ratio, 1.4 for air
Δt	=	nondimensional time-step size
δ_{ij}	=	Kronecker delta function

I. Introduction

UNSTEADY separation control is a challenging area for numerical simulations [1]. This problem was again confirmed at the computational fluid dynamics (CFD) Validation on Synthetic Jets and Turbulent Separation Control Workshop sponsored by NASA Langley Research Center in March 2004 [2]. The participants that attempted the workshop's third case had trouble accurately matching experimental results in the hump wake. Although multiple turbulence-modeling methodologies were used, no one employed a large-eddy simulation (LES) approach. The present work will determine if a high-order LES can achieve better agreement with experimental flow physics.

The experimental work for the NASA workshop [3,4] was based on a geometry and methodology similar to that used by Seifert and Pack [1,5,6]. Both uncontrolled and controlled flow conditions were investigated with multiple data acquisition methods, including streamwise and spanwise pressure taps, extensive 2-D and 3-D particle image velocimetry (PIV), limited hot-wire and pitot tube measurements, and oil-film flow visualization. The main objective of the NASA workshop was to develop a comprehensive database of experiments employing flow control for subsequent validation and comparison with CFD methods.

The workshop participants employed a multitude of steady/unsteady Reynolds-averaged Navier–Stokes RANS methodologies [2]. Some of these groups also used more advanced techniques, including detached eddy simulations, hybrid RANS–LES methods, and direct numerical simulation (DNS). The current authors also participated in this workshop using a high-order numerical scheme for both the RANS equations and the turbulence model [7]. Unfortunately, independently of the approach employed, none of the participants achieved excellent agreement with the experimental data. Even the DNS did not achieve any better results than the RANS-based methodologies. Some of the disagreement with experimental results was due to wind-tunnel blockage caused by end plates, which led to a uniform shift in the surface pressure coefficient magnitude. Mostly, the disagreement was due to the reliance on RANS models, which are generally unreliable for accurately simulating separated flows.

None of the groups participating in the workshop used a pure LES to solve the problem. The current authors have previously employed a high-order scheme, described in the Numerical Method section, for multiple LES/DNS simulations, including a supersonic cavity flowfield [8], a supersonic compression ramp [9,10], channel flow [11], transitional flow over a circular cylinder [11], an airfoil [12,13], and a low-pressure turbine [14,15]. Based on the success of these previous works, the current research will investigate if better agreement can be achieved with experimental data using LES.

The next two sections of this paper describe the governing equations and numerical scheme, respectively. Finally, details of the simulations and results are presented. The Results section will cover the comparison of the flow control cases to RANS and experimental data. Additionally, a study investigating the effectiveness of the flow control as a function of the oscillatory blowing-and-suction amplitude is discussed.

II. Governing Equations

The governing LES equations are the unsteady, three-dimensional, compressible, unfiltered Navier–Stokes equations. After transforming the equations from Cartesian coordinates to general body-fitted curvilinear coordinates, the equations can be cast into strong conservation-law form as

Presented as Paper 5017 at the 35th AIAA Fluid Dynamics Conference and Exhibit, Toronto Ontario, Canada, 6–9 June 2005; received 23 January 2006; revision received 3 April 2007; accepted for publication 10 June 2007.

*Senior Scientist, Ohio Aerospace Institute. Associate Fellow AIAA.
†Senior Research Aerospace Engineer, Computational Sciences Branch. Associate Fellow AIAA.
‡Technical Area Leader, Computational Sciences Branch. Associate Fellow AIAA.

$$\frac{\partial}{\partial t}\left(\frac{\mathbf{Q}}{J}\right)+\frac{\partial}{\partial \xi}\left(\mathbf{F}-\frac{1}{Re_c}\mathbf{F}_v\right)+\frac{\partial}{\partial \eta}\left(\mathbf{G}-\frac{1}{Re_c}\mathbf{G}_v\right)+\frac{\partial}{\partial \zeta}\left(\mathbf{H}-\frac{1}{Re_c}\mathbf{H}_v\right)=0 \tag{1}$$

where t is the time; ξ, η, and ζ are the computational coordinates; $\mathbf{Q}$ is the vector of dependent variables; $\mathbf{F}$, $\mathbf{G}$, and $\mathbf{H}$ are the inviscid flux vectors; and $\mathbf{F}_v$, $\mathbf{G}_v$, and $\mathbf{H}_v$ are the viscous flux vectors. The vector of dependent variables is

$$\mathbf{Q}=[\rho\ \ \rho u\ \ \rho v\ \ \rho w\ \ \rho E]^T \tag{2}$$

and the vector fluxes are given by

$$\mathbf{F}=\frac{1}{J}\begin{bmatrix}\rho U\\ \rho uU+\xi_x p\\ \rho vU+\xi_y p\\ \rho wU+\xi_z p\\ \rho EU+\xi_{x_i}u_i p\end{bmatrix},\qquad \mathbf{G}=\frac{1}{J}\begin{bmatrix}\rho V\\ \rho uV+\eta_x p\\ \rho vV+\eta_y p\\ \rho wV+\eta_z p\\ \rho EV+\eta_{x_i}u_i p\end{bmatrix}$$
$$\mathbf{H}=\frac{1}{J}\begin{bmatrix}\rho W\\ \rho uW+\zeta_x p\\ \rho vW+\zeta_y p\\ \rho wW+\zeta_z p\\ \rho EW+\zeta_{x_i}u_i p\end{bmatrix} \tag{3}$$

$$\mathbf{F}_v=\frac{1}{J}\begin{bmatrix}0\\ \xi_{x_i}\tau_{i1}\\ \xi_{x_i}\tau_{i2}\\ \xi_{x_i}\tau_{i3}\\ \xi_{x_i}(u_j\tau_{ij}-q_i)\end{bmatrix},\qquad \mathbf{G}_v=\frac{1}{J}\begin{bmatrix}0\\ \eta_{x_i}\tau_{i1}\\ \eta_{x_i}\tau_{i2}\\ \eta_{x_i}\tau_{i3}\\ \eta_{x_i}(u_j\tau_{ij}-q_i)\end{bmatrix}$$
$$\mathbf{H}_v=\frac{1}{J}\begin{bmatrix}0\\ \zeta_{x_i}\tau_{i1}\\ \zeta_{x_i}\tau_{i2}\\ \zeta_{x_i}\tau_{i3}\\ \zeta_{x_i}(u_j\tau_{ij}-q_i)\end{bmatrix} \tag{4}$$

where

$$U=\xi_{x_i}u_i,\qquad V=\eta_{x_i}u_i,\qquad W=\zeta_{x_i}u_i \tag{5}$$

$$E=\frac{T}{\gamma(\gamma-1)M_\infty^2}+\frac{1}{2}(u^2+v^2+w^2) \tag{6}$$

In the preceding expressions, u, v, and w are the Cartesian velocity components; ρ is the density; p is the pressure; T is the temperature; E is the total specific energy; and J is the Jacobian of the coordinate transformation. All length scales were nondimensionalized by the hump chord c, and dependent variables were normalized by their reference values, except for p, which was nondimensionalized by $\rho_\infty u_\infty^2$. Components of the stress tensor and heat flux vector may be expressed as

$$\mathbf{q}_i=-\left[\frac{1}{(\gamma-1)M_\infty^2}\right]\left(\frac{\mu}{Pr}\right)\frac{\partial \xi_j}{\partial x_i}\frac{\partial T}{\partial \xi_j} \tag{7}$$

$$\tau_{ij}=\mu\left(\frac{\partial \xi_k}{\partial x_j}\frac{\partial u_i}{\partial \xi_k}+\frac{\partial \xi_k}{\partial x_i}\frac{\partial u_j}{\partial \xi_k}-\frac{2}{3}\delta_{ij}\frac{\partial \xi_l}{\partial x_k}\frac{\partial u_k}{\partial \xi_l}\right) \tag{8}$$

The Sutherland law for the molecular viscosity coefficient μ and the perfect gas relationship

$$p=\frac{\rho T}{\gamma M_\infty^2} \tag{9}$$

were also employed. Stokes's hypothesis for the bulk viscosity coefficient has also been invoked.

In the standard compressible LES approach, the preceding equations are filtered by employing a grid filter function and introducing Favre-filtered variables [16]. The resulting equations are similar to those preceding but include additional subgrid-scale stress and heat flux terms that must be modeled. In this work, an implicit LES (ILES) method is used that relies on the high-order nondispersive spatial filter of the scheme in lieu of a subgrid stress model [17] to prevent pileup of energy at the high wave numbers not resolved on the mesh.

The RANS simulations use equations similar to those already described. A full discussion of the RANS approach and the $k-\epsilon$ model used for the eddy viscosity can be found in [7].

III. Numerical Method

The solver used for these computations advances the solution in time using a second-order implicit subiterative Beam–Warming algorithm [18]. The implicit approximate-factorization Beam–Warming algorithm may be written in delta form as

$$\begin{aligned}&\left[\frac{1}{J}+\left(\frac{2\Delta t}{3}\right)\delta_{\xi 2}\left(\frac{\partial \mathbf{F}^p}{\partial \mathbf{Q}}-\frac{1}{Re_c}\frac{\partial \mathbf{F}_v^p}{\partial \mathbf{Q}}\right)\right]J\\ &\quad\times\left[\frac{1}{J}+\left(\frac{2\Delta t}{3}\right)\delta_{\eta 2}\left(\frac{\partial \mathbf{G}^p}{\partial \mathbf{Q}}-\frac{1}{Re_c}\frac{\partial \mathbf{G}_v^p}{\partial \mathbf{Q}}\right)\right]J\\ &\quad\times\left[\frac{1}{J}+\left(\frac{2\Delta t}{3}\right)\delta_{\zeta 2}\left(\frac{\partial \mathbf{H}^p}{\partial \mathbf{Q}}-\frac{1}{Re_c}\frac{\partial \mathbf{H}_v^p}{\partial \mathbf{Q}}\right)\right]\Delta\mathbf{Q}\\ &=-\left(\frac{2\Delta t}{3}\right)\left[\left(\frac{1}{2\Delta t}\right)\left(\frac{3\mathbf{Q}^p-4\mathbf{Q}^n+\mathbf{Q}^{n-1}}{J}\right)\right.\\ &\quad+\delta_\xi\left(\mathbf{F}^p-\frac{1}{Re_c}\mathbf{F}_v^p\right)+\delta_\eta\left(\mathbf{G}^p-\frac{1}{Re_c}\mathbf{G}_v^p\right)\\ &\quad\left.+\delta_\zeta\left(\mathbf{H}^p-\frac{1}{Re_c}\mathbf{H}_v^p\right)\right]\end{aligned} \tag{10}$$

where $\partial\mathbf{F}/\partial\mathbf{Q}$, $\partial\mathbf{G}/\partial\mathbf{Q}$, and $\partial\mathbf{H}/\partial\mathbf{Q}$, are flux Jacobians; $\mathbf{Q}$ is the solution vector; and δ represents the spatial difference operator. Newton-like subiterations [19] are incorporated into the scheme to recover temporal accuracy and stability properties of the algorithm due to errors introduced by linearization, factorization, and explicit updating of boundary conditions and overset grid interfaces. Subiterations also permit the use of the more efficient diagonal form [20] of the implicit algorithm while retaining time accuracy. The subiterate is given by $\Delta\mathbf{Q}=\mathbf{Q}^{p+1}-\mathbf{Q}^p$, where p denotes the number of subiterations. For the first solver application ($p=1$), $\mathbf{Q}^p=\mathbf{Q}^n$, where n is the solution time level. With subsequent subiterations $\mathbf{Q}^{p+1}\to\mathbf{Q}^{n+1}$. Based on previous unsteady flow computations, three applications of the solver per time step are typically found to be sufficient to recover second-order time accuracy.

The implicit portion of the algorithm uses second-order-accurate three-point backward differencing for the time derivative and second-order central finite difference approximations for the spatial derivatives [denoted with the subscript 2 in Eq. (10)]. Nonlinear artificial dissipation terms (not shown) are appended to the implicit operator to enhance stability. The spatial derivatives on the right-hand side of Eq. (10) use compact-difference operators that recover higher-order spatial accuracy with subiterations.

The high-order spatial derivatives on the right-hand side of the governing equation are discretized using the compact finite difference scheme of Lele [21], which can attain spectral-like resolution. Using the tridiagonal subset of this scheme, the spatial derivative of any scalar f, such as a metric, flux component, or flow variable, can be obtained by solving the system

$$\alpha\left(\frac{\partial f}{\partial \xi}\right)_{i-1}+\left(\frac{\partial f}{\partial \xi}\right)_i+\alpha\left(\frac{\partial f}{\partial \xi}\right)_{i+1}=a\left(\frac{f_{i+1}-f_{i-1}}{2}\right)+b\left(\frac{f_{i+2}-f_{i-2}}{4}\right) \tag{11}$$

where α, a, and b determine the spatial properties of the algorithm. The present investigation employed a compact fourth-order scheme corresponding to $\alpha = \frac{1}{4}$, $a = \frac{3}{2}$, and $b = 0$.

Dispersion-error characteristics and truncation error of these schemes are discussed in detail in [21,22]. Also discussed in [22] are descriptions of the higher-order one-sided formulas used near boundaries.

To control numerical instabilities, a general high-order (up to tenth-order) low-pass Padé-type spatial filter was incorporated into the compact-difference scheme [23]. These nondispersive spatial filters were demonstrated as superior to explicit artificial viscosity, especially on generalized curvilinear meshes. The filter is applied to the solution vector $\mathbf{Q}$ in each of the three computational directions following each subiteration. The filtered values of the solution vector are obtained by solving the tridiagonal system

$$\alpha_f \check{\mathbf{Q}}_{i-1} + \check{\mathbf{Q}}_i + \alpha_f \check{\mathbf{Q}}_{i+1} = \sum_{n=0}^{N} \frac{a_n}{2} (\mathbf{Q}_{i+n} + \mathbf{Q}_{i-n}) \qquad (12)$$

where $\check{\mathbf{Q}}$ represents the filtered value of $\mathbf{Q}$, and α_f is a free parameter for this family of filters, which must remain in the range $-0.5 < \alpha_f < 0.5$. Higher values of α_f correspond to less dissipative filters. The coefficients a_n in Eq. (12) are summarized in [22]. The choice of N provides a $2N$th-order filter. On uniform meshes, these filters preserve constant functions, completely eliminate the odd–even mode decoupling, and do not amplify waves [24]. Low-pass filtering provides dissipation at the high modified wave numbers *only* when the spatial discretization already exhibits significant dispersion errors, whereas non-spectral-based artificial viscosity and upwind-biased schemes introduce dissipation across a wide range of wave numbers. The present investigation employed a sixth-order filter with $\alpha_f = 0.4$.

Filtering near any domain boundary requires the implementation of one-sided high-order Padé-type formulas, as discussed in [22,23]. Unlike the interior filter, the one-sided high-order filters can amplify wave amplitudes for a certain range of wave numbers. To eliminate this undesirable amplification behavior, higher values of α_f are sometimes required near boundaries [25].

The preceding components are implemented in a parallel scheme based on domain decomposition and an overset grid methodology. The overset grid implementation uses interpolation for the overlapping blocks and direct injection of coincident points. The methodology is used in conjunction with the message passing interface (MPI) library for interblock communication. The resulting MPI code was successfully ported to several parallel platforms. Additional background on the parallel compact solver is covered in detail in [11].

IV. Details of the Computation

The hump geometry simulates the upper surface of a 20%-thick Glauert–Goldschmied airfoil. The wall-mounted hump has a chord length of 0.4200 m, a maximum height of 0.0537 m, and a span of 0.5842 m. A slot is located at approximately 65% chord for flow control. An outline of the body, slot, and plenum can be seen in the computational mesh (Fig. 1). The flow conditions for the computation were $M_\infty = 0.10$ and $Re_c = 2.0 \times 10^5$. The experiment used for comparison was performed at $Re_c = 9.36 \times 10^5$. The lower Reynolds number was chosen to maintain LES resolution requirements and to keep computational costs to an acceptable level. Because the Reynolds number was reduced by a factor of 5, only qualitative agreement with experimental data should be anticipated.

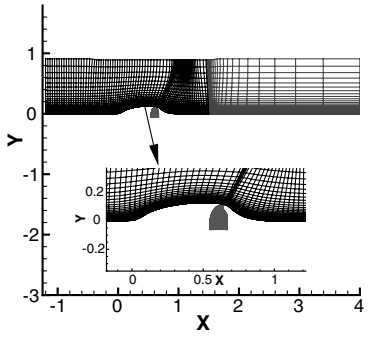

Fig. 1 Grid for the wall-mounted hump.

The experimental domain for the wind tunnel and hump, nondimensionalized by the length of the hump, extended from $-2.14 \le x \le 4.0$ in the streamwise direction, from $0.0 \le y \le 0.9090$ in the normal direction (representing the bottom and top walls of the wind tunnel), and from $0.0 \le z \le 1.39$ in the spanwise direction. The hump was located between $0.0 \le x \le 1.0$. To keep the mesh size manageable, the inflow of the computational domain was located at $x = -1.2$ and the spanwise domain was limited to 20% chord.

A. Computational Mesh

The wall-mounted-hump and upper-wind-tunnel-surface definitions corrected for blockage were provided by NASA. To ensure that the LES was adequately resolved, the fine grid was developed to have $1.6 \le \Delta x^+ \le 60$, $\Delta y^+_{\text{wall}} = 1$, and $\Delta z^+ = 20$, where Δx^+, Δy^+, and Δz^+ are mesh spacings in wall units based on the inflow profile. To meet these requirements, the streamwise grid distribution had 798 equally spaced points from $x = -1.2$ to 1.5, except for clustering ten slot lengths upstream and downstream of the slot. Twenty additional points with rapid stretching were appended in the streamwise direction from $x = 1.5$ to 4.0. This region with rapid stretching in conjunction with the numerical filter provides a nonreflecting outflow buffer domain. The normal grid distribution had 151 points and was generated using a hyperbolic tangent function with a normal wall spacing of $\Delta n = 6.4 \times 10^{-5}$. Finally, the spanwise direction extended from $0.0 \le z \le 0.2$, which corresponds to about three inflow-boundary-layer heights. The span was modeled using 161 evenly spaced points, with four additional grid points added to enforce periodicity. Thus, the final mesh size for the hump and interior of the wind tunnel was $818 \times 151 \times 165$ points in the streamwise, normal, and spanwise directions, respectively. The slot and plenum were represented using a $41 \times 133 \times 165$ mesh in the streamwise, normal, and spanwise directions, respectively. Both meshes enforced orthogonality to all surfaces and were generated using Gridgen [26]. The final grid, given in Fig. 1, displays every tenth line in the streamwise direction and every third line in the normal direction.

To assess the LES solutions' grid dependency, a coarse mesh was generated by removing every other point in each coordinate direction. The resulting coarse mesh had significantly larger spacing than is normally acceptable for LES, but results can still be used to assess the level of resolution. For discussion purposes, the term LES will be used in the Results section to refer to the fine-mesh results, and the term VLES (very-large-eddy simulation) will be used to refer to the coarse-mesh results. It is critical to note that previous researchers [27] have determined that as mesh resolution is increased for an LES, new modes continue to be resolved until the DNS level is reached, and so the concept of a grid-independent solutions does not really exist in LES.

B. Initial and Boundary Conditions

Boundary conditions used in the simulations include isothermal no-slip walls for the lower plate and hump surface, inviscid-wall boundary conditions for the top of the wind tunnel, prescribed velocities and density with pressure extrapolated at the inflow, and pressure fixed to its freestream value, with all other outflow variables extrapolated at the outflow. Periodicity was enforced in the spanwise direction. The slot/plenum walls enforced no-slip isothermal conditions, and the bottom of the cavity treated all quantities as an inviscid wall. The v component of velocity at the bottom of the cavity imposed three different boundary conditions. For the baseline (no flow control) case, v was set to zero at the bottom of the cavity. For the suction case, $v = -0.012475$ was prescribed to match the given mass flow rate of 0.01518 kg/s through the 0.5842-m-wide slot. For

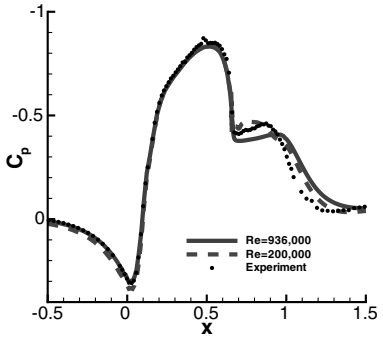

Fig. 2 Effect of the Reynolds number on the pressure coefficient for 2-D RANS.

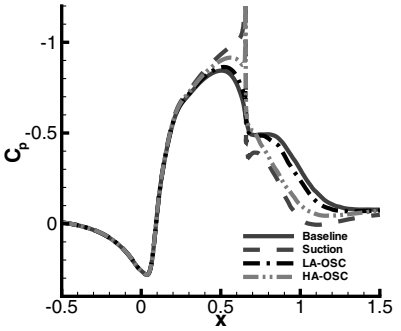

Fig. 4 Mean pressure coefficient comparison between baseline and flow control LES simulations.

the oscillatory blowing-and-suction case, the velocity was defined by $v = A\sin(\omega t)$, where $A = 9.39 \times 10^{-3}$ and $\omega = 2\pi f$. The amplitude of the forcing, A, was assigned this value to reproduce the experimental maximum slot velocity of 26.6 m/s. The forcing frequency f was prescribed to the experimental value of 138.5 Hz.

Initial conditions at the inflow were set to a steady-state RANS solution superimposed with flow disturbances from a flat-plate LES. A RANS solution was employed at $x = -1.2$ because no experimental data were available for this location, only at $x = -2.14$, the experimental domain inflow. The RANS solutions come from the work discussed in [7]. Further discussion of the current inflow implementation can be found in [28].

The 3-D hump LES computation was initialized by interpolating the previous baseline LES solution used in [28] onto the current mesh. The flow was advanced 20,000 time steps before collecting time-averaged statistics. This was sufficient time for the flow to adjust to the addition of the slot used for flow control. Flow statistics were collected for the next 100,000 time steps.

V. Results

LES results for the hump cases both with and without flow control are compared with experimental data [3,4] and RANS solutions. A full description of the RANS approach and comparison with experimental data for this case can be found in [7]. The current 2-D RANS solutions were obtained on the coarse mesh from [7] at the lower Reynolds number of $Re_c = 2.0 \times 10^5$. Because the governing equations, boundary conditions, and excitation frequency were nondimensionalized in the flow solver, changing the Reynolds number does not alter the reduced excitation frequency from $F^+ = 0.77$ or the oscillatory flow momentum coefficient from $C_\mu = 0.11\%$. To determine the effects of using a lower Re_c, a second-order-accurate RANS simulation was performed at both the experimental and LES Reynolds numbers. For the lower-Reynolds-number RANS simulation, the inflow profile was adjusted to account for changes in the incoming boundary layer. Figure 2 shows the hump surface pressure coefficient C_p for both RANS simulations and experimental data. Lowering the Reynolds number resulted in virtually no change in C_p over the front portion of the hump. In the recirculation region downstream of the slot, lowering the Reynolds number increased the magnitude of C_p by approximately 15%. This difference diminished before flow reattachment. Even with the visible difference of C_p in the wake, the reattachment location for the RANS simulations differ by less than 1% chord. Based on these RANS results, it appears that lowering the Reynolds number does not significantly alter the flow characteristics.

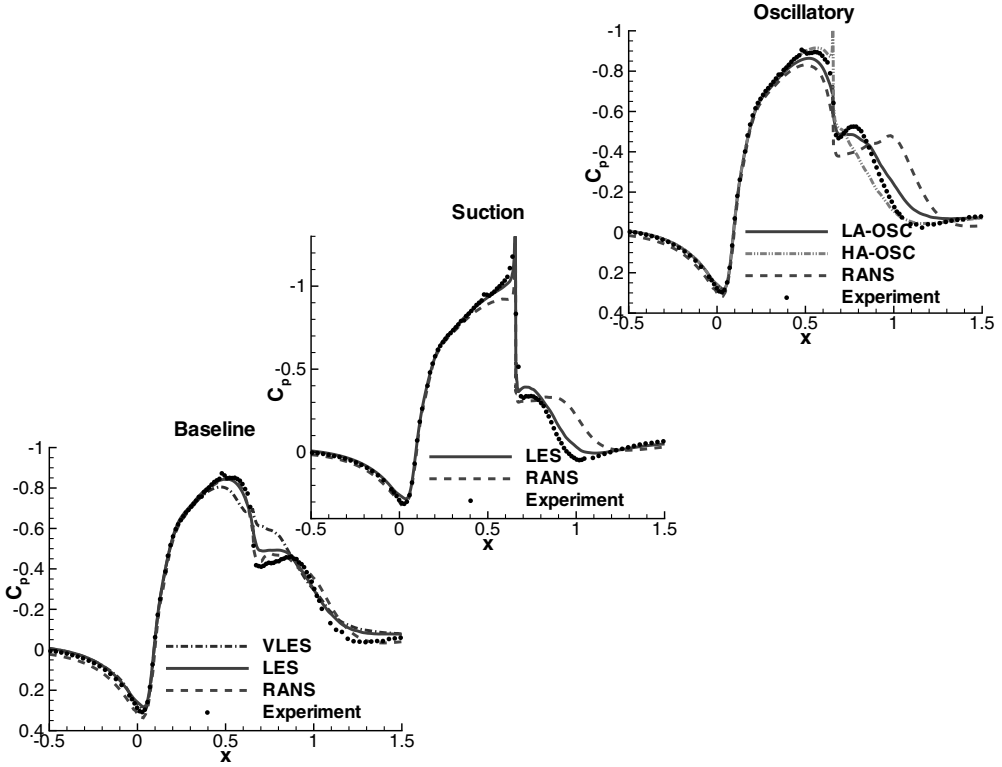

Fig. 3 Mean pressure coefficient comparison between LES, RANS, and the experiment.

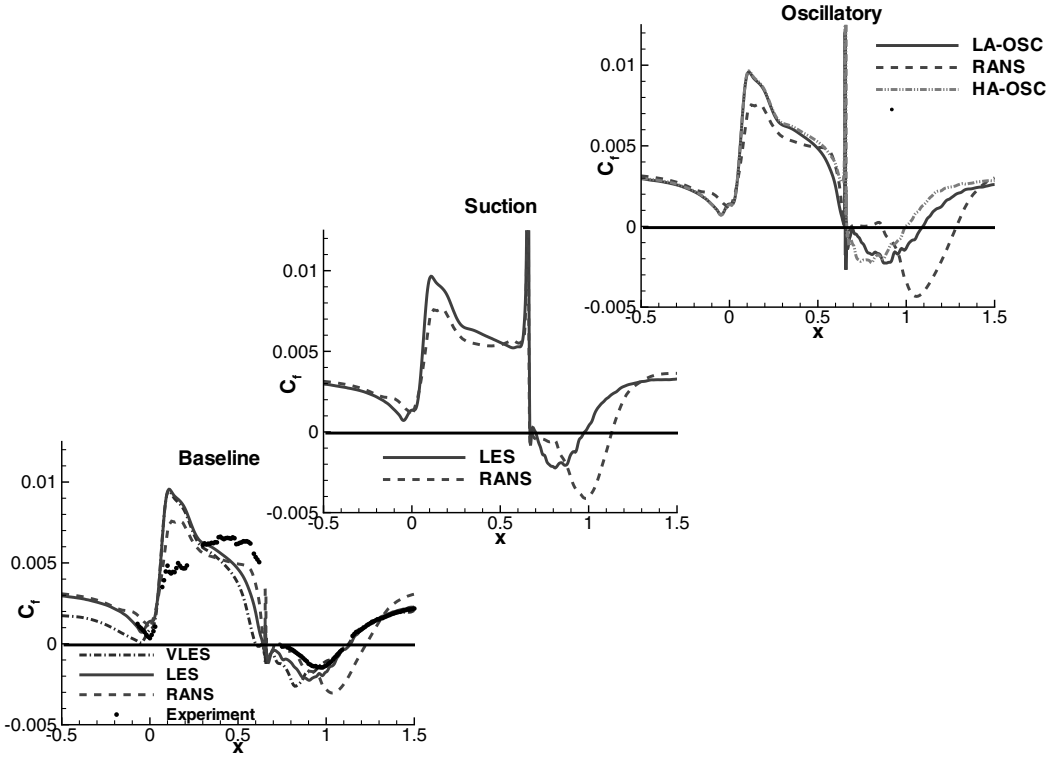

Fig. 5 Mean skin-friction coefficient comparison between LES, RANS, and the experiment.

The large-eddy simulations completed at the lower Reynolds number demonstrated good qualitative agreement with experimental data for the baseline and suction cases. However, the oscillatory blowing-and-suction case exerted significantly less flow control than that observed in the wind tunnel. Experimental studies [4] investigated ranges of the oscillatory flow momentum coefficient C_μ for various reduced excitation frequencies F^+ and Reynolds numbers to determine their effect on form drag. The results suggest that larger forcing amplitudes exert more control on the separated region and reduce drag. The largest value of C_μ tested that did not have a nonzero value of F^+ was $C_\mu \approx 0.75\%$. This value corresponds to a 250% increase in the forcing amplitude for the oscillatory flow control. Because at the lower Reynolds number the LES did not agree with experimental data as well as the other flow control case, the LES was repeated using this larger oscillatory forcing amplitude to demonstrate that it could reproduce this experimental trend by exerting more control on the separated region. Hereafter, the oscillatory blowing-and-suction LES case using experimental conditions is referred to as LA-OSC and the higher-amplitude forced LES is referred to as HA-OSC. In the following results, all mean profiles (C_p, C_f, $\bar{u}$, $\bar{v}$, etc.) described were both spanwise and temporally averaged.

A. Time-Mean Flowfields

A comparison of the VLES and LES mean surface pressure coefficient C_p with experiment and RANS results is shown in Fig. 3. The experimental data, LES, and RANS solutions all display a large peak near the midchord of the hump, which is associated with the flow acceleration in that region. The second noticeable flow feature is the small plateau region downstream of the flow control slot located at 65% chord, which is characteristic of flow separation. All of the LES solutions display the same qualitative character and magnitude seen in the experiment upstream of the flow control slot. The VLES in the baseline case and RANS solutions for the suction and oscillatory cases have a slightly lower magnitude than that observed in the experiment. In the recirculation region downstream of the hump, the baseline and flow control LES results show very similar physical characteristics and magnitudes to those of the experimental data. The variations in C_p in this region reflect the slight differences in the lengths of the separation bubbles. Also note that the baseline and LA-OSC solutions have a slightly flatter profile in the near wake of the slot. For the HA-OSC result, the plateau in the separated region virtually disappeared due to the larger amount of control exerted on the separated region. For both the steady-suction and oscillatory flow control cases, the LES solutions match the experimental data better than the RANS solutions in the wake.

A comparison of the baseline coarse-mesh VLES and fine-mesh LES C_p profiles indicate that the finer LES mesh has an acceptable level of grid resolution. As clearly seen in Fig. 3, the fine-grid LES solution has significantly better agreement with experimental data over the midchord and wake of the hump.

A comparison of the surface pressure coefficient between the baseline and flow control cases is shown in Fig. 4. Upstream of the

Table 1 Hump flow-reattachment-location summary

Case	Experiment	LES	RANS
Baseline	1.11 ± 0.003	1.139	1.23
Suction	0.94 ± 0.005	0.978	1.14
LA-OSC	0.98	1.097	1.29
HA-OSC	0.98	0.997	-

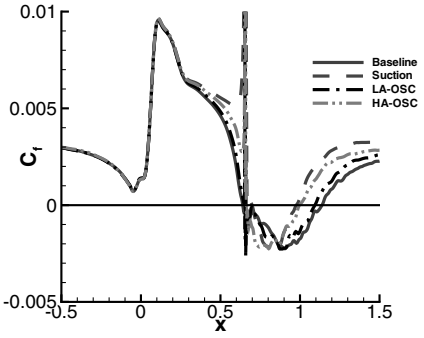

Fig. 6 Mean skin-friction coefficient comparison between baseline and flow control LES simulations.

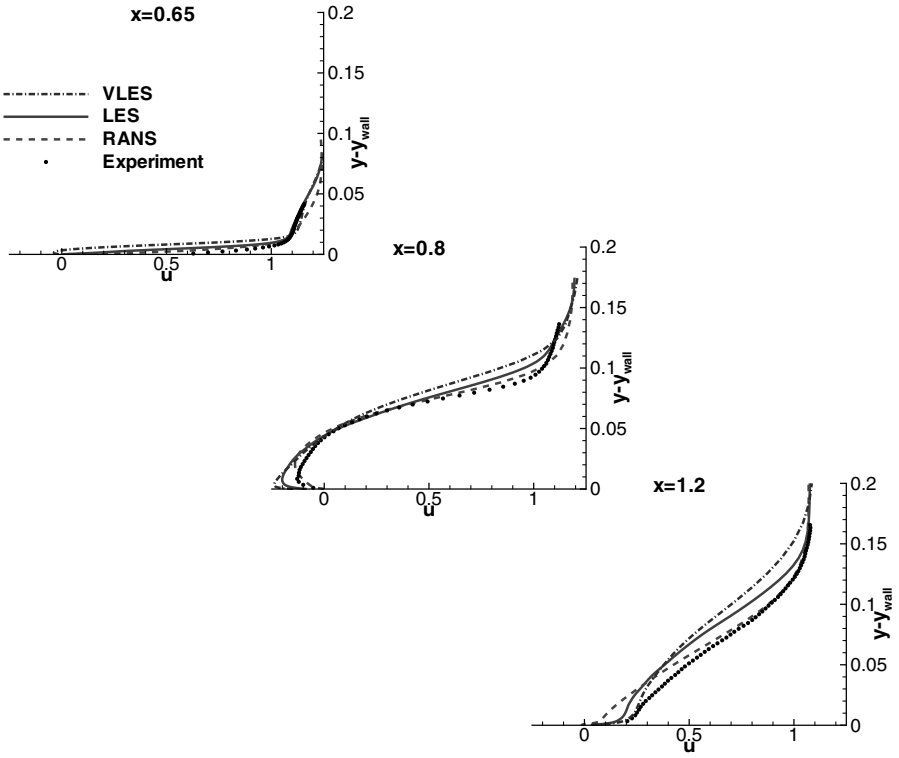

Fig. 7 Baseline case: mean u-velocity profile comparisons at $x = 0.65$, 0.8, and 1.2.

slot, the suction case displays a higher peak in C_p. This results from the flow acceleration near the slot stemming from the steady mass removal from the flow. Downstream of the slot, the effect of steady suction develops a shorter plateau, indicating a smaller recirculation region. The baseline and the LA-OSC cases appear to be very similar along the entire surface of the hump. The HA-OSC case develops a higher magnitude than the LA-OSC case upstream of the slot. In the recirculation region, it has a smaller magnitude that approaches the steady-suction solution.

A comparison of the mean skin-friction coefficient C_f for the LES, RANS, and experiment is shown for the different cases in Fig. 5. Also shown in the figure is a line at $C_f = 0$ to delineate between attached and separated flow. Unfortunately, experimental data were only available for the baseline case, and so LES results for the flow control cases are limited to comparison with RANS. Of all the flow quantities examined in this study, the skin-friction coefficient is the only result that significantly changed when the Reynolds number was reduced. The baseline RANS, VLES, and LES solutions display a sharp peak near the leading edge of the hump that does not exist in the experimental results. Also, the numerical simulations underpredict C_f over the midportion of the hump. Performing two RANS simulations in which only Re_c is changed verifies that the peak in C_f over the front portion of the hump results solely from lowering the Reynolds number. Although this is not shown in the current work, it can be seen by comparing the current RANS result with the solution at the higher Re_c in [7]. Once separation occurs, the baseline LES skin-friction coefficient displays a dramatic improvement in agreement with the experimental data. Both the VLES and LES results display the proper qualitative character and magnitude in the recirculation and downstream recovery regions. The RANS solutions display only a qualitative agreement with the experiment in the hump wake.

The LES and RANS simulations employing flow control show C_f characteristics similar to the baseline case. Increasing the amplitude of the oscillatory flow control provided more control on the separation bubble and reduced the size of the recirculation region, as seen in the HA-OSC result.

Coarse- and fine-mesh LES solutions for the baseline case display significant differences in C_f only upstream of the hump. This difference reflects the sensitivity that C_f has to mesh resolution in the boundary layer. Over the chord and wake of the hump, increasing grid resolution results in relatively small changes in C_f.

A summary of flow reattachment locations is given in Table 1. Because the LES and RANS simulations were performed at a lower Reynolds number, perfect agreement with the experimental separation and reattachment locations should not be expected. The VLES result is not shown in Table 1 because it is underresolved and was only applied to the baseline case. Reattachment for the VLES

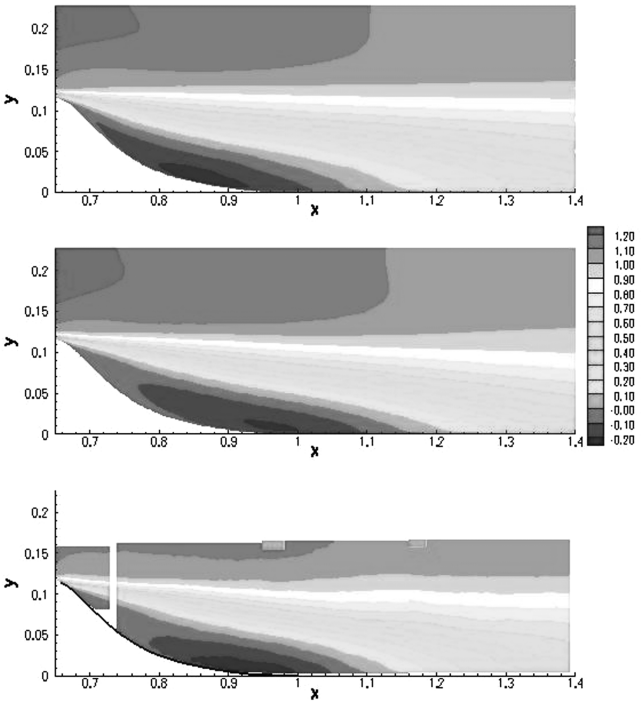

Fig. 8 Baseline case: comparison of LES (top), RANS (middle), and experimental PIV (bottom) u-velocity contours.

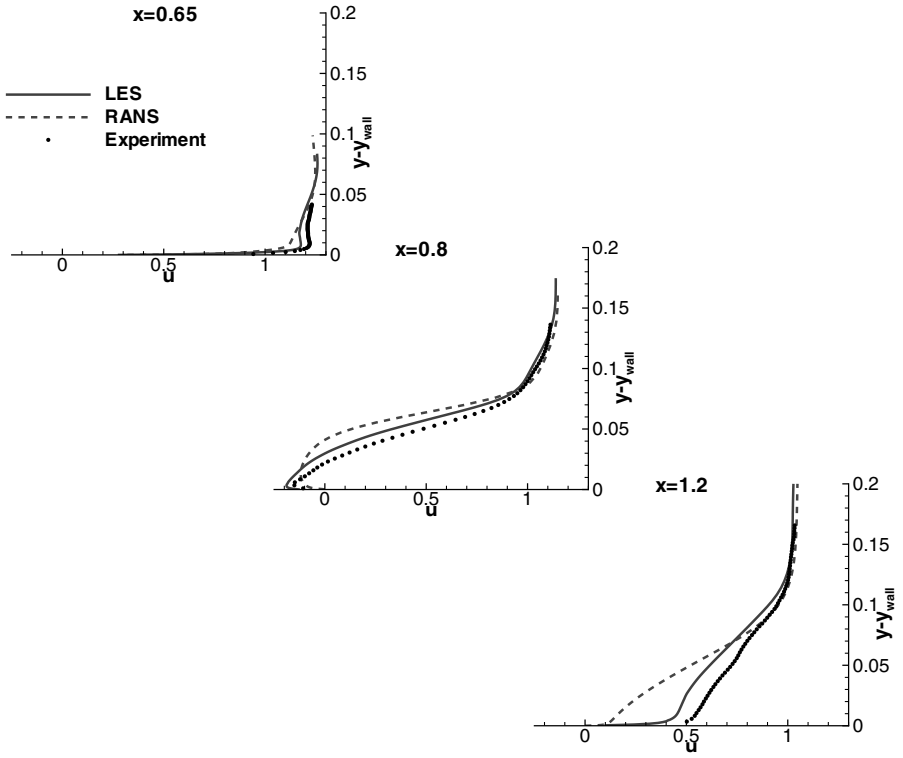

Fig. 9 Suction case: mean u-velocity profile comparisons at $x = 0.65$, 0.8, and 1.2.

occurred at $x = 1.13$, at nearly the same location as the more resolved LES. The baseline and steady-suction fine-mesh LES reattachment locations were only about 3 and 4%, respectively, downstream of the experimental values. The LA-OSC case was approximately 10% downstream of the experimental results, and the HA-OSC case was within 2% of the reattachment location. The RANS solutions were anywhere from 10–32% downstream of the experimental observations. Overall, the LES results predicted smaller separation-bubble lengths that were closer to experimental values.

A direct comparison of C_f for the baseline and flow control LES cases is shown in Fig. 6. The LES solutions are virtually identical for the front portion of the hump. Just upstream of the slot, the steady-suction case displays a significant increase in the skin-friction coefficient, due to the favorable pressure gradient that accelerates the flow and develops a higher-velocity gradient near the wall. The effects of steady suction are also clearly evident downstream of the hump, as seen by the significant reduction in the length of the separation bubble. As already discussed, the LA-OSC case causes minimal changes in the separation-bubble length and in C_f, but by increasing the amplitude of the oscillatory forcing, the separation length can be significantly decreased.

Mean u-velocity profiles at three streamwise locations for the baseline flow are shown in Fig. 7. The three profiles are extracted from the flow at $x = 0.65$, 0.8, and 1.2, corresponding to a point just before the slot, one location in the separated flow region, and another station right after flow reattachment. The first location slightly upstream of the slot and separation, $x = 0.65$, shows the LES profile agreeing well with the experimental u-velocity profile. The RANS solution overshoots in the upper portion of the boundary layer. The VLES profile already displays reverse flow because separation occurred upstream of the slot. Downstream in the recirculation region, $x = 0.8$, the VLES, LES, and RANS solutions have a qualitative shape and magnitude very similar to the experimental profile. Some slight differences do exist in the profiles, such as the maximum reverse-flow velocity attained by the VLES and LES is slightly larger than that observed experimentally. At $x = 1.2$, just downstream of reattachment, the LES and experimental profiles display similar characteristics near the wall because reattachment occurred upstream of the current location. The RANS profile still has a small separation region at the wall. In the outer portion of the boundary layer, the RANS solution recovers more quickly than the VLES and LES solutions.

Comparisons of the mean u-velocity contours for RANS, LES, and experimental PIV data are depicted in Fig. 8. The mean u-velocity RANS, LES, and experimental PIV contour plots display very similar flow features. The LES and experiment have a stronger reverse flow than RANS just off the wall between $0.8 < x < 1.0$. The main difference between the LES and experiment is that the region of fastest reverse flow in the LES is approximately 5% chord further upstream than that observed in the experiment. The RANS solution

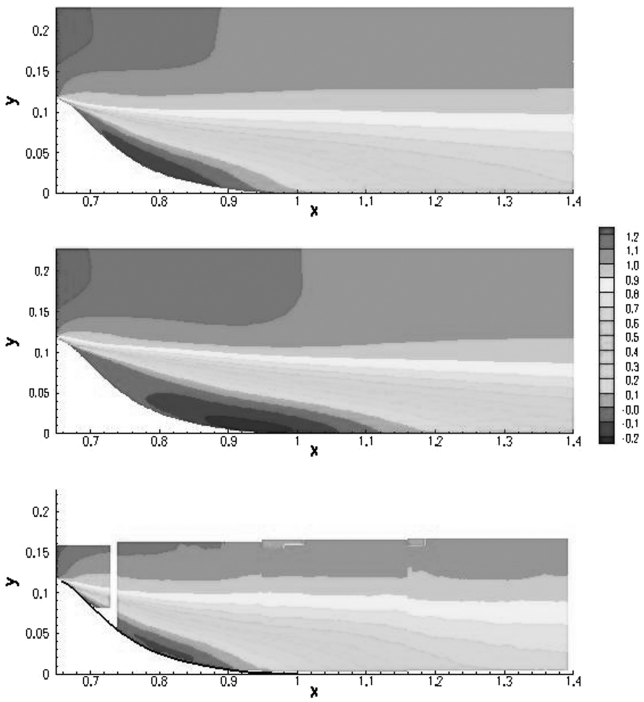

Fig. 10 Suction case: comparison of LES (top), RANS (middle), and experimental PIV (bottom) u-velocity contours.

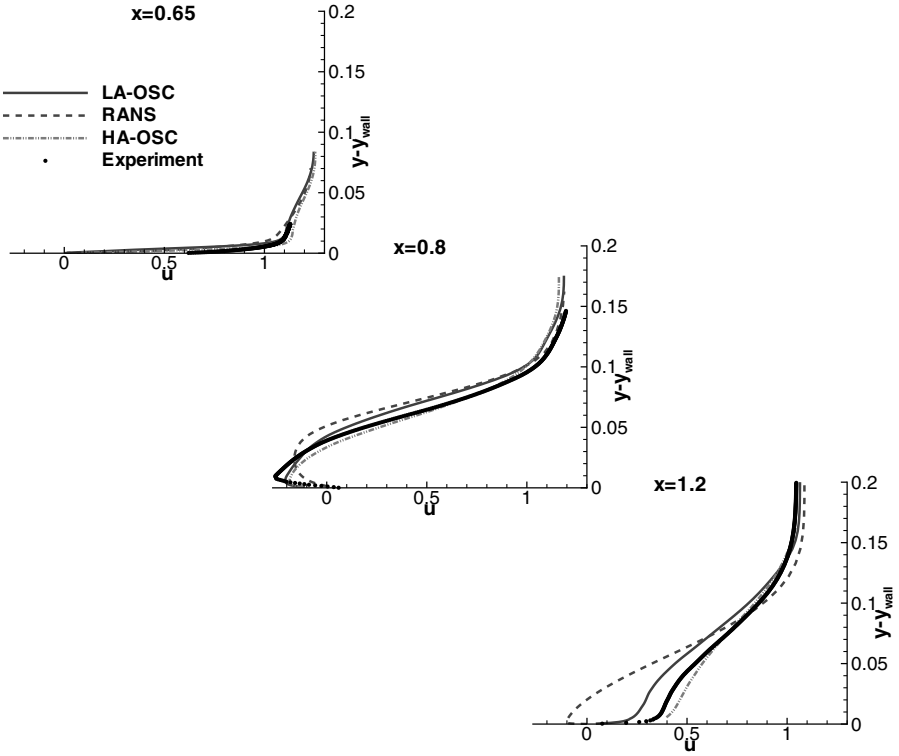

Fig. 11 Oscillating blowing-and-suction case: mean u-velocity profile comparisons at $x = 0.65$, 0.8, and 1.2.

clearly shows a longer separation bubble than the experiment and LES results.

The mean u-velocity profiles at the same three streamwise locations are shown in Fig. 9 for the case of steady suction. The LES $\bar{u}$-velocity profiles have the same qualitative shape as the experiment at all stations shown. At $x = 0.65$, both the LES and RANS mean u-velocity profiles are not quite as full as the experimental data. In the middle of the separation bubble at $x = 0.8$, both numerical approaches display good agreement with the experimental data. Finally, at $x = 1.2$ downstream of reattachment, neither the LES nor RANS streamwise-velocity profiles have recovered to the extent of the experiment, due to delayed reattachment. However, because the LES solution reattaches sooner than RANS, it is significantly closer to the experimental observations.

Figure 10 shows a comparisons of LES, RANS, and experimental time-mean u-velocity contours for the entire separated flow region. The contour plots show similar flow characteristics between the LES and the experiment. The size and length of the separation bubbles have significant similarity; however, the LES is slightly longer and displays a stronger reverse flow. The RANS solution also displays qualitative agreement with the experimental data, although the separation region is significantly larger and the flow reattaches further downstream.

Mean u-velocity profiles for the oscillatory blowing-and-suction cases are shown in Fig. 11. The oscillatory flow control displays trends similar to those seen in the baseline case. Of specific interest in this case is the impact of increasing the amplitude of the flow control, which can be seen by comparing the LA-OSC to the HA-OSC results. The higher-amplitude forcing resulted in very minor changes upstream of the slot at $x = 0.65$, a thinner reverse flow region at $x = 0.8$, and a more recovered profile after reattachment at $x = 1.2$.

The comparisons of LA-OSC, RANS, and experimental time-mean u-velocity contours for oscillatory flow control are shown in Fig. 12. This comparison displays more differences between the experiment and the LES and RANS solutions than seen in the baseline and steady-suction cases. The LA-OSC has a slightly larger separation bubble than the experiment. The RANS approach performed poorly in this case, as seen by the significantly larger recirculation region that extends approximately 30% chord downstream of the experimental result.

Finally, to better evaluate the effectiveness of the flow control, both the steady-suction and oscillatory flow control solutions are compared with the baseline LES case in Fig. 13. Overall, there is a consistent trend that the streamwise-velocity profiles are fuller for the cases using flow control. As seen in the other flow quantities, the LA-OSC case introduced smaller changes from the baseline case than the HA-OSC. Steady suction, on the other hand, produced more visible effects at the given stations. Slightly upstream of the slot, the effects of steady suction are clearly visible in the fuller velocity profile. Also,

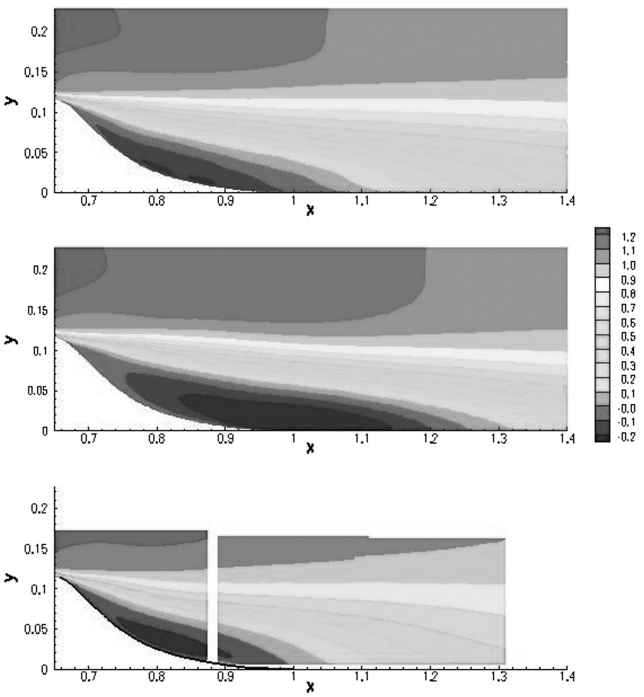

Fig. 12 Oscillating blowing-and-suction case: comparison of LA-OSC LES (top), RANS (middle), and experimental PIV (bottom) u-velocity contours.

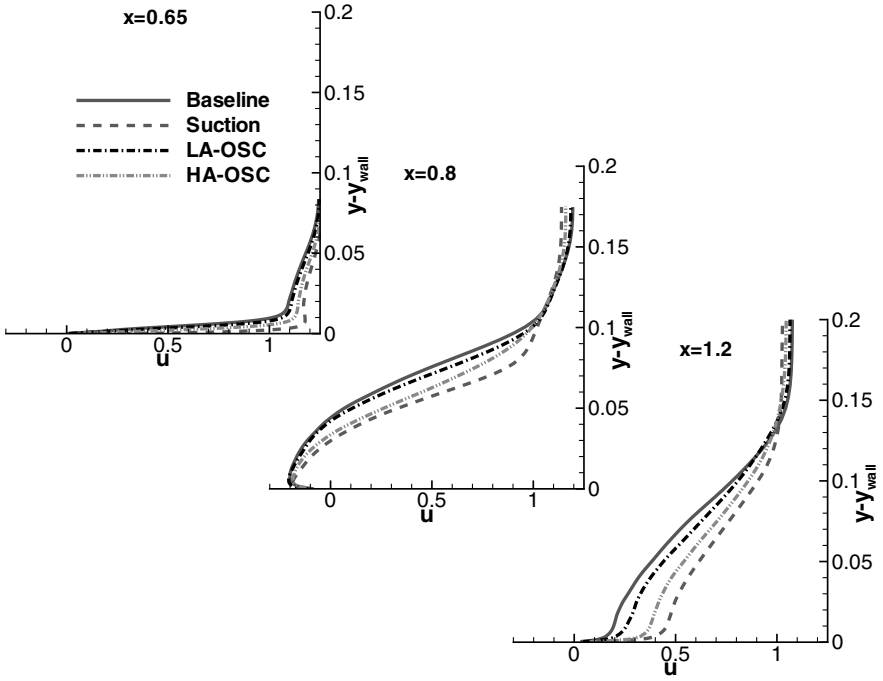

Fig. 13 LES mean u-velocity profile comparisons at $x = 0.65$, 0.8, and 1.2.

inside the separated flow region, the height at which the streamwise velocity becomes positive is noticeably smaller than in the other cases. At the last station, $x = 1.2$, the mean u-velocity profile for the suction and HA-OSC cases display a more recovered profile than the baseline and LA-OSC cases, due to the earlier flow reattachment.

B. Unsteady Flowfield Features

Comparisons of LES, RANS, and experimental turbulent kinetic energy (TKE) profiles at $x = 0.65$, 0.8, and 1.2 for the baseline and flow control cases are shown in Figs. 14–16. For purposes of the current discussion, the TKE is defined as $k = 0.5(\overline{u'u'} + \overline{v'v'})$. The $\overline{w'w'}$ component is not included in this definition because it was not available from the experimental data.

The LES and RANS baseline-case solutions have profiles that qualitatively agree with the experiment data at the locations observed. The LES TKE magnitude at $x = 0.65$ is slightly over six times larger than the experiment near the wall. The VLES result is almost 50% larger than the LES magnitude. The RANS solution also displays this overshoot, although not quite as pronounced. The larger magnitude is likely related to the unsteady motion of the flow separation point, which is very near the current location. The

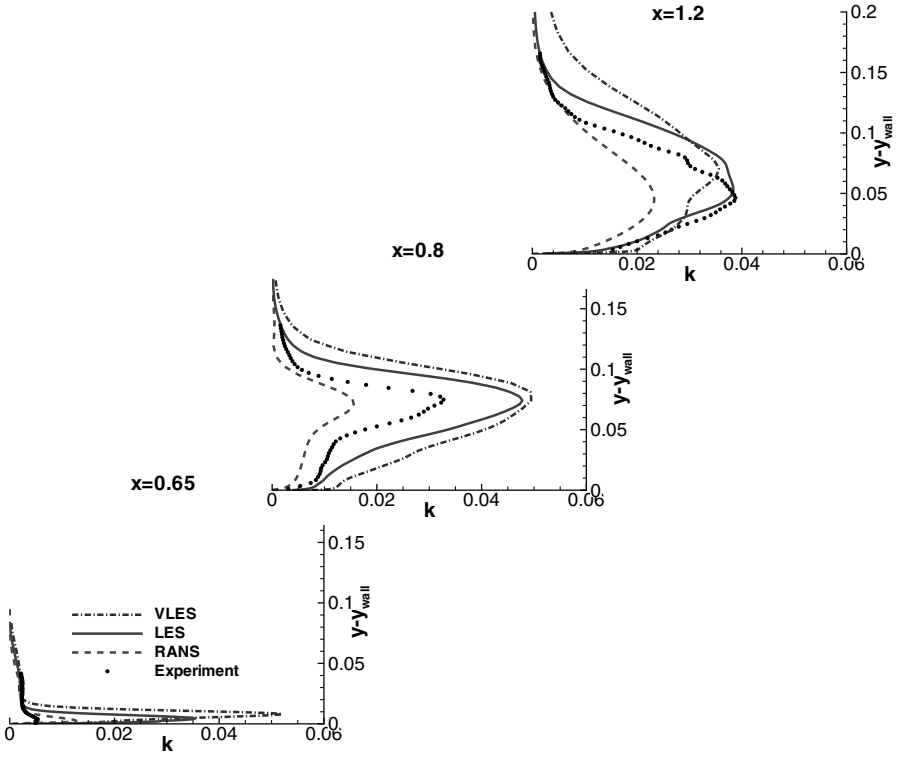

Fig. 14 Baseline case: mean turbulent kinetic energy profile comparisons at $x = 0.65$, 0.8, and 1.2.

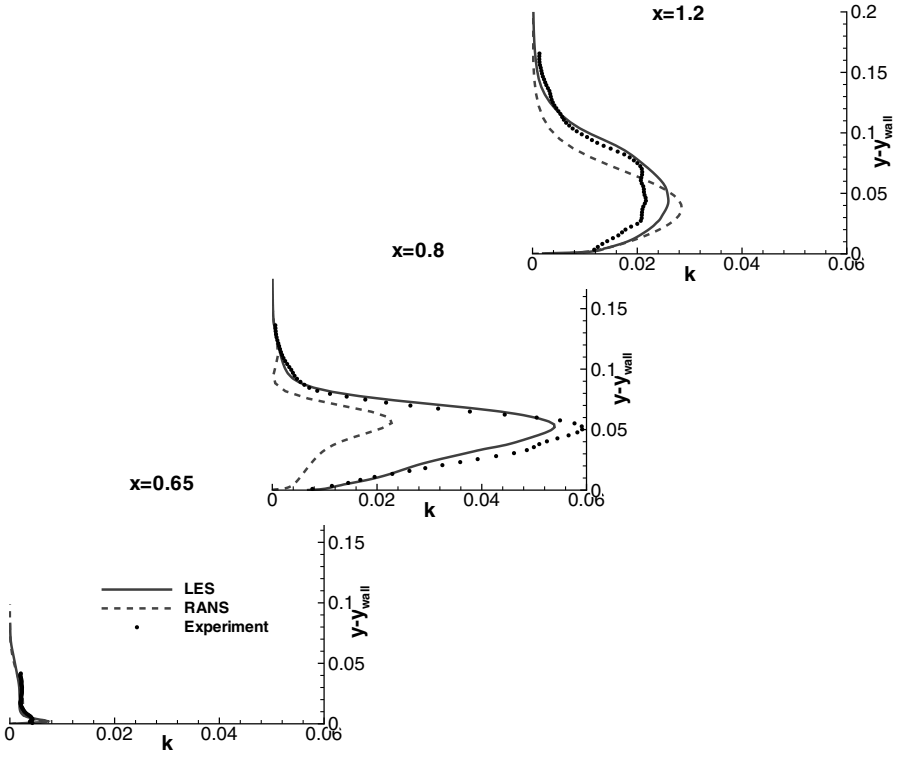

Fig. 15 Suction case: mean turbulent kinetic energy profile comparisons at $x = 0.65$, 0.8, and 1.2.

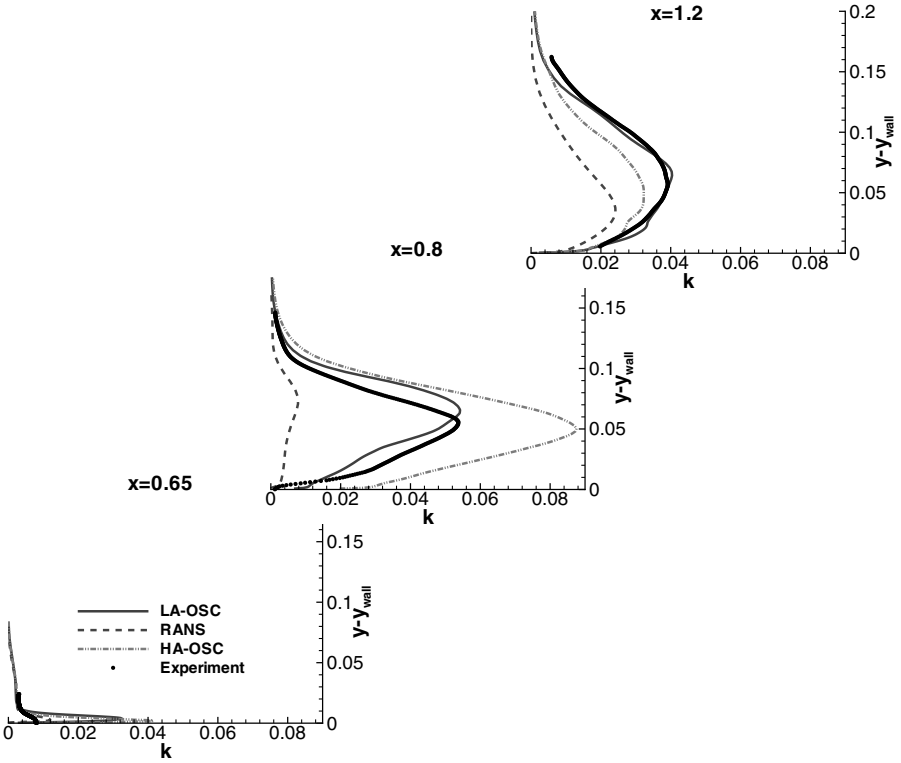

Fig. 16 Oscillating blowing-and-suction case: mean turbulent kinetic energy profile comparisons at $x = 0.65$, 0.8, and 1.2.

experiment does not display this character because flow separation occurs downstream of this location at the higher Reynolds number. Agreement between the LES and experiment improves downstream of the slot and is best at $x = 1.2$. The VLES profiles are again similar to the LES, except the peak magnitude occurs higher in the boundary layer. Although the RANS predictions have the correct qualitative shape, they are smaller in magnitude than the LES and experimental results at these downstream locations.

For the case of steady suction, the LES TKE profiles have a magnitude and qualitative shape very similar to the experimental data at all three locations. RANS solutions also develop similar profiles, but lack the proper magnitude downstream of separation.

For the LA-OSC case, the LES TKE profiles display the same shape and magnitude as the experiment at 0.8 and 1.2. As in the baseline case, the magnitude at $x = 0.65$ is significantly larger than the experiment. The HA-OSC simulation displays larger TKE

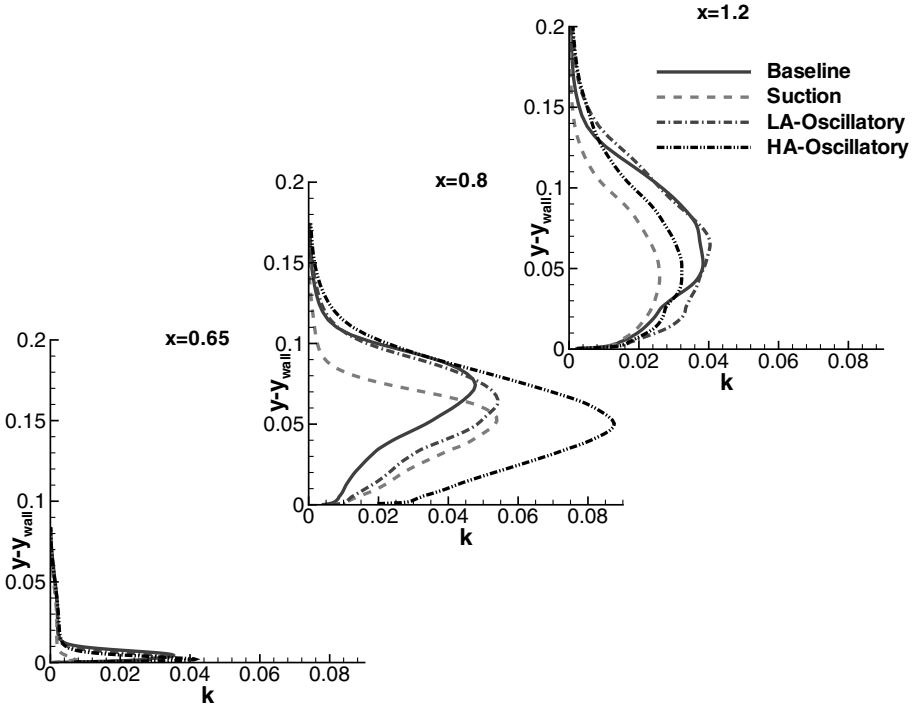

Fig. 17 Mean turbulent kinetic energy profile comparison between baseline and flow control LES simulations.

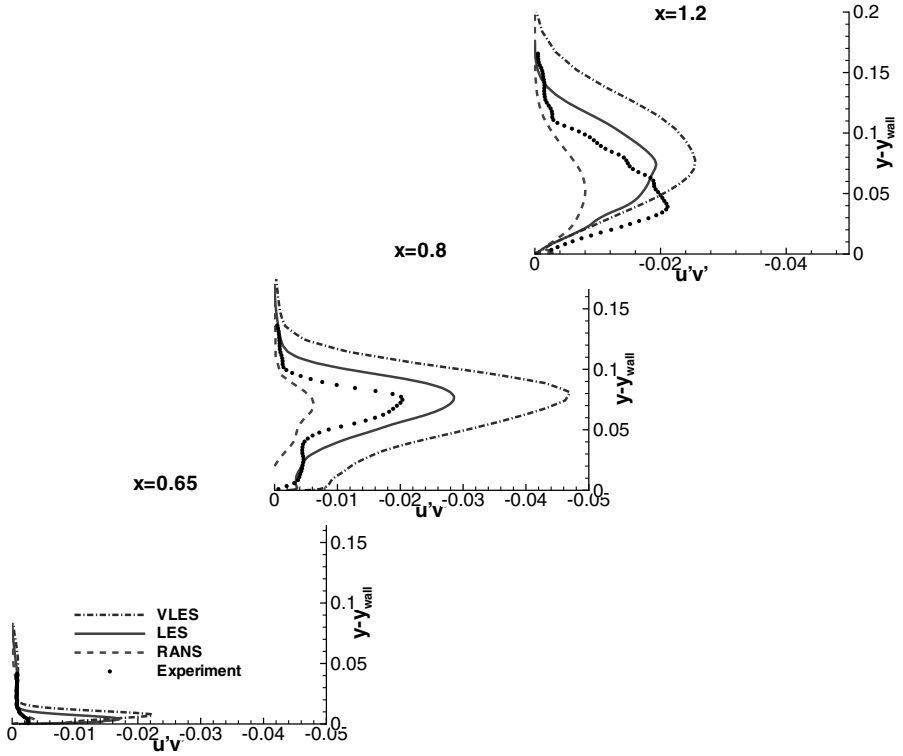

Fig. 18 Baseline case: mean Reynolds stress profile comparisons at $x = 0.65$, 0.8, and 1.2.

amplitudes than the LA-OSC case at the two most upstream stations. For oscillatory flow control, the RANS approach develops less TKE than the experiment and LES downstream of the slot.

Figure 17 shows the comparison of the TKE between the LES baseline and flow control cases. The steady-suction profile at $x = 0.65$ has a significantly smaller TKE peak near the wall because the flow is attached and more stable. Also notable at this location is that the HA-OSC simulation displays a significantly higher peak magnitude. At $x = 0.8$, the TKE profile for steady suction is slightly larger than the baseline case. It also peaks closer to the wall because the separation bubble is thinner. The effects of the higher forcing amplitude continue to be present in the HA-OSC profile, which has a magnitude twice the baseline value. At the last station, $x = 1.2$, the oscillatory flow control solutions have recovered to the baseline magnitude and shape. The steady-suction profile also has the same qualitative shape as the baseline solution, but only two-thirds the magnitude.

The baseline-case Reynolds stress profiles, shown in Fig. 18, display the same basic behavior observed in the TKE at the three stations. At $x = 0.65$, the LES has a larger magnitude than the

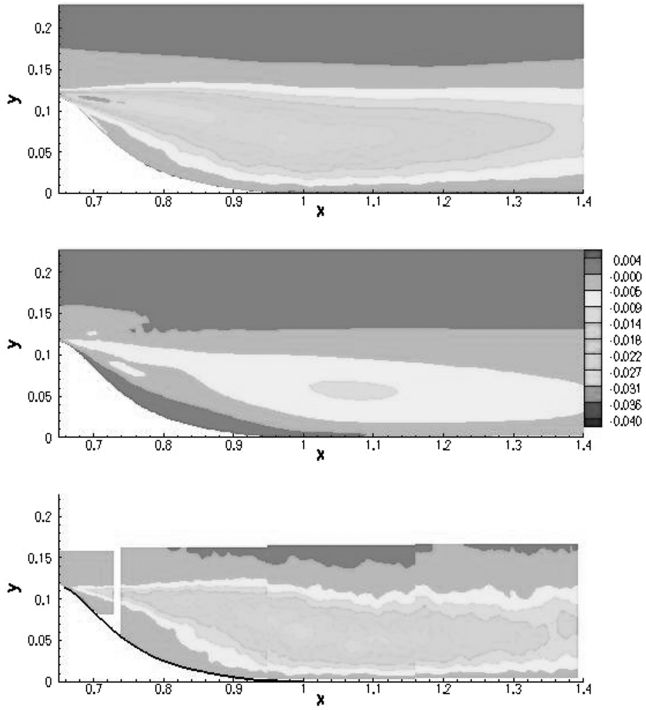

Fig. 19 Baseline case: comparison of LES (top), RANS (middle), and experimental PIV (bottom) Reynolds stress contours.

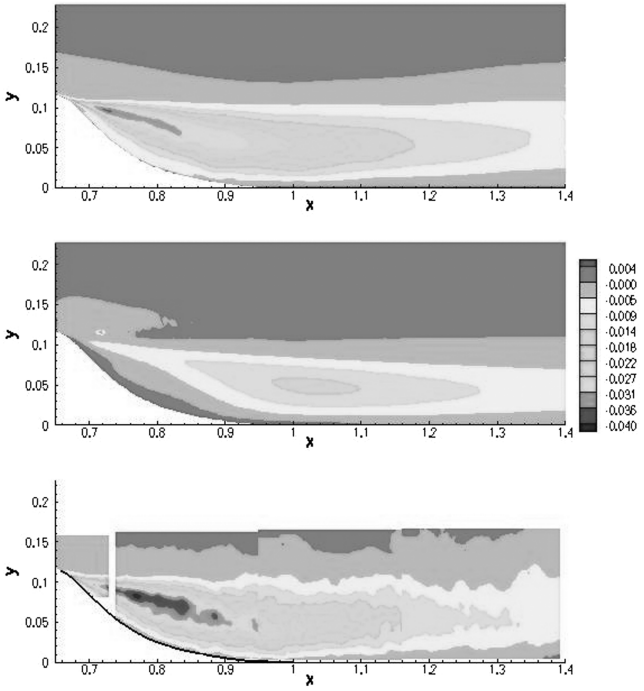

Fig. 21 Suction case: comparison of LES (top), RANS (middle), and experimental PIV (bottom) Reynolds stress contours.

experimental profile. Downstream at $x = 0.8$, the LES $\overline{u'v'}$ profile has the same shape as the experiment, but a slightly larger magnitude. At $x = 1.2$, the Reynolds stress profiles have the same character as the experiment, but the LES has a slightly smaller magnitude and the peak occurs slightly higher in the boundary layer. The VLES profiles are similar to the LES, except they are up to 40% larger in magnitude. RANS results have the same qualitative trends as the experiment at all three locations, but the magnitude was smaller at all locations. The contour plots comparing Reynolds stresses downstream of the hump are shown in Fig. 19. Here, it can be clearly seen that the LES developed a smaller, thinner region of minimum Reynolds stress that was located further upstream than in the experiment. The RANS solution does not reach the same level of Reynolds stresses seen in the experiment and LES. The RANS minimum magnitude region is significantly smaller and is located further downstream than in both the LES and experiment.

Reynolds stress profiles for steady-suction results are compared in Fig. 20. The LES qualitatively reproduces the experimental Reynolds stresses well at all three locations. Even the magnitudes

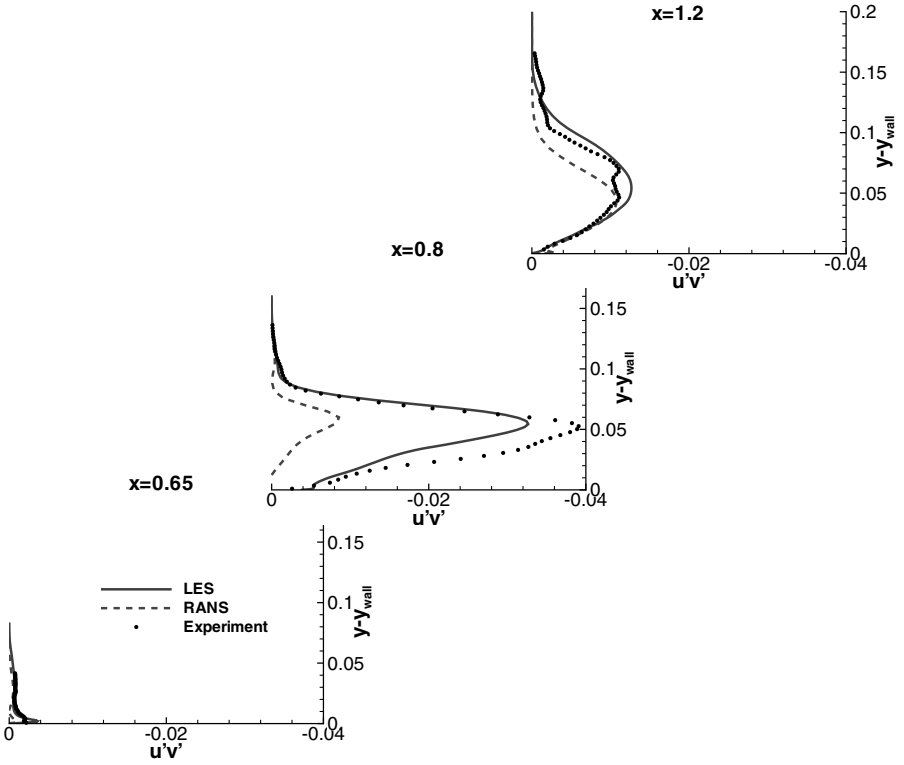

Fig. 20 Suction case: mean Reynolds stress profile comparisons at $x = 0.65$, 0.8, and 1.2.

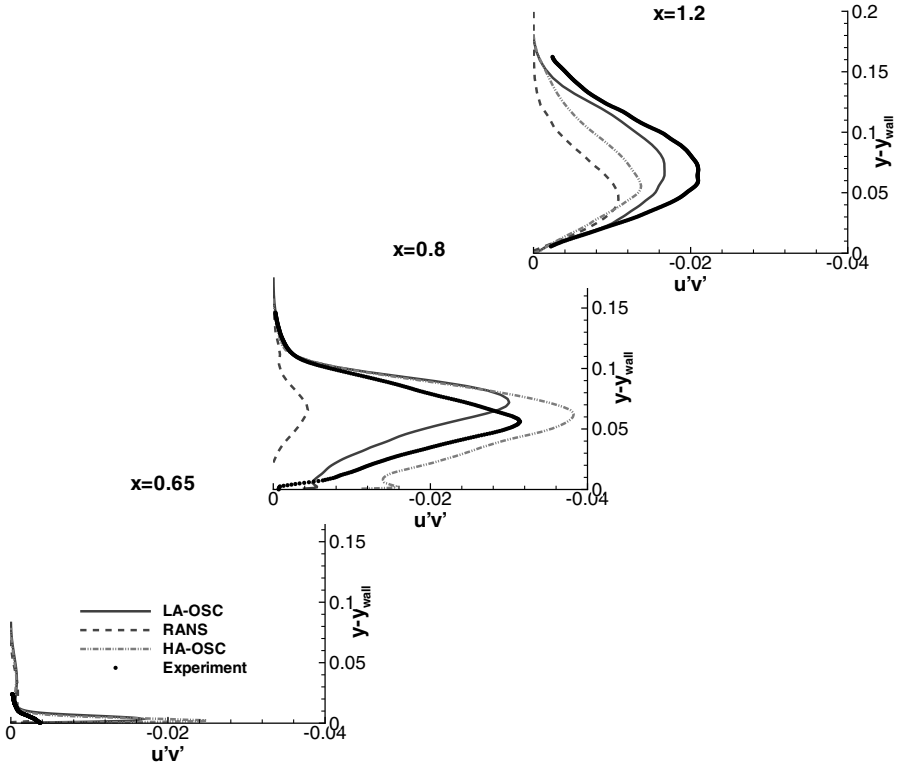

Fig. 22 Oscillating blowing-and-suction case: mean Reynolds stress profile comparisons at $x = 0.65$, 0.8, and 1.2.

agree well, except at $x = 0.8$, for which the LES has only three-fourths of the experimental value. RANS also predicts the proper magnitude and shape at the slot and in the recovery region. In the separation bubble, the magnitude is underpredicted by RANS by about a factor of 4. Figure 21 shows the larger picture of the Reynolds stresses downstream of the hump by means of a contour plot. Overall, the LES and experimental contours have the same qualitative shape and magnitude, except the LES did not develop the lowest magnitude of Reynolds stress seen in the experiment. The RANS contours display a smaller Reynolds stress that is located about a quarter-chord further downstream.

For the oscillatory blowing-and-suction case, the Reynolds stress profiles (see Fig. 22) show the same basic behavior at the three stations as that seen in the TKE. Upstream of the slot, both LES simulations overpredict the magnitude of the experimental Reynolds stress. The maximum magnitude of the HA-OSC Reynolds stress profile near the slot is about 50% larger than that of the baseline LA-OSC. Inside the separated region, the LA-OSC profile has the same shape and magnitude as the experiment. Two minor differences that exist are a small peak in the LA-OSC profile near the wall that is not seen in the experimental data, and the maximum magnitude of the second peak is higher in the boundary layer than in the experiment. The HA-OSC profile has a larger magnitude than the LA-OSC solution throughout the boundary layer. At $x = 1.2$, the Reynolds stress profiles have the same character, but both the LA-OSC and HA-OSC cases have smaller magnitudes than the experiment. In this case, RANS clearly underpredicts the Reynolds stresses in both profiles after the slot. The contour plots of Reynolds stress downstream of the hump are shown in Fig. 23. Here, the LA-OSC LES developed a smaller, thinner region of minimum Reynolds stress that was located further upstream than in the experiment. The RANS simulation fails to develop the minimum magnitude seen in both the experiment and LES. RANS also locates the leading edge of a similar magnitude region over 40% chord further downstream.

Finally, a comparison of the LES Reynolds stress profiles between the baseline and flow control cases is shown in Fig. 24. The trends for the Reynolds stress are very similar to those described in the TKE.

Instantaneous streamwise-velocity contours in the x–y plane and isosurfaces of constant vorticity magnitude for the oscillatory suction and blowing case are shown in Fig. 25. Note that this figure was stretched by a factor of 2 in the spanwise direction to enhance visualization. The flow in this picture is moving in the direction of the positive x axis. The turbulent boundary layer with multiple spanwise structures can be seen approaching the hump. These turbulent structures diminish as the flow accelerates over the midportion of the hump. After separation, the effect of pulsing is evident in the large spanwise structures that convect downstream.

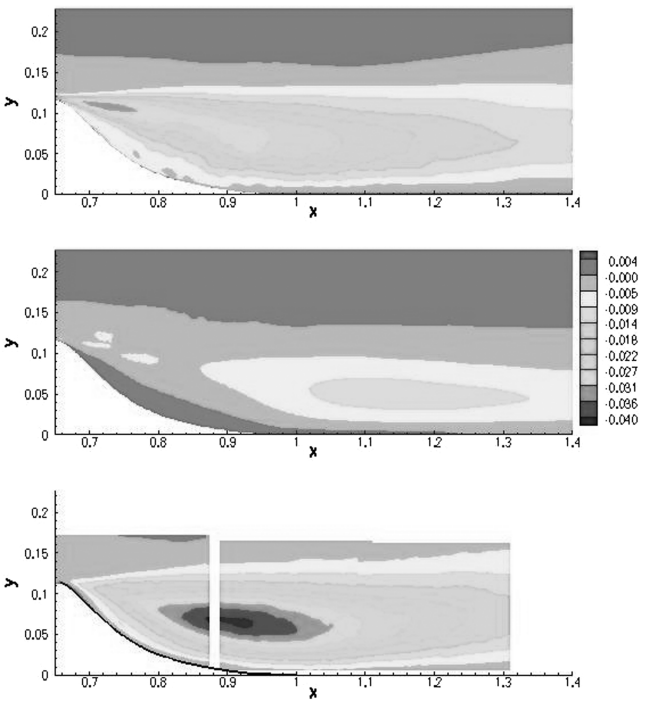

Fig. 23 Oscillating blowing-and-suction case: comparison of LA-OSC LES (top), RANS (middle), and experimental PIV (bottom) Reynolds stress contours.

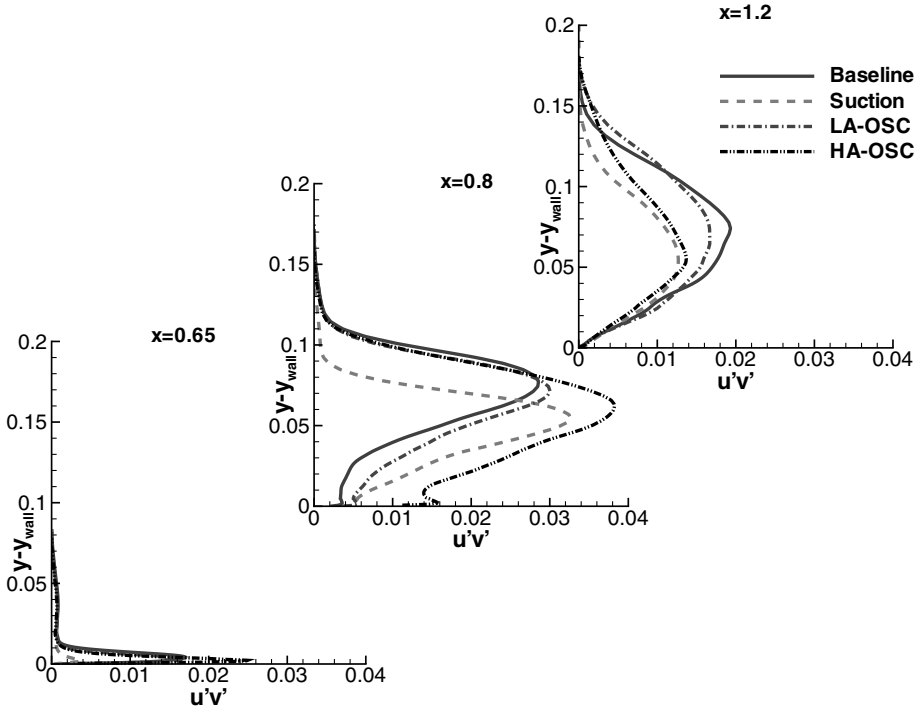

Fig. 24 Mean Reynolds stress comparison between baseline and flow control LES simulations.

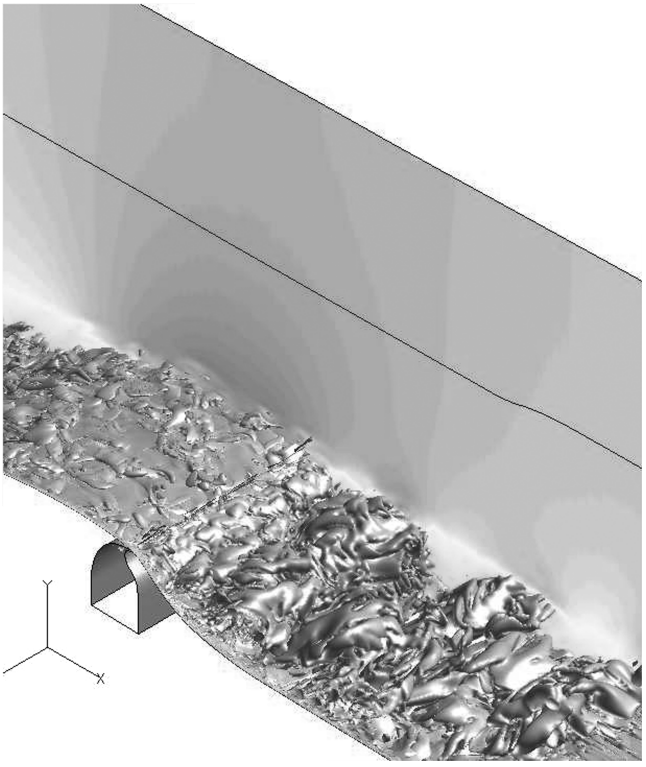

Fig. 25 Oscillating blowing-and-suction LES: instantaneous u-velocity contours and isosurface of constant vorticity magnitude.

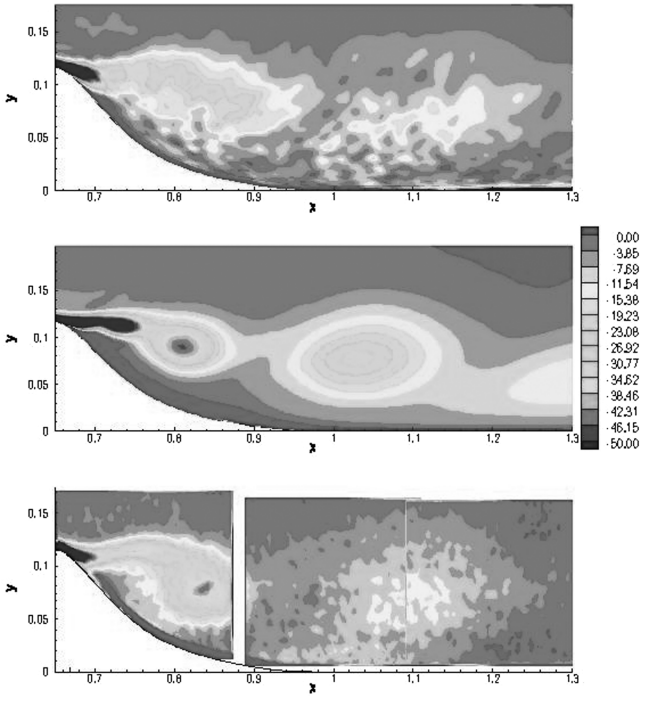

Fig. 26 Oscillating blowing-and-suction case; comparison between LA-OSC LES (top), RANS (middle), and experimental PIV (bottom) phase-averaged z-vorticity contours at $\Theta = 0$ deg.

Phase-averaged comparisons between the LA-OSC LES, RANS, and experimental results are shown in Figs. 26–29, which depict the z-vorticity flow history of the oscillatory suction and blowing at $\theta = 0$, 90, 180, and 270 deg, respectively. The phase angle $\theta = 90$ deg corresponds to maximum blowing and $\theta = 270$ deg corresponds to maximum suction in the oscillatory cycle. Overall, the LA-OSC LES, RANS, and experiment have good agreement in the general characteristics of the flow, including size and locations of the vortex generated, even though there are slight differences in magnitude. The RANS results display more coherent vortices throughout the blowing-and-suction cycle that do not dissipate as rapidly in the wake.

Figures 30–33 show comparisons of LES, RANS and experimental u-velocity and Reynolds stress contours of the near slot region corresponding to the four phase angles already described. Near the slot, the LES and RANS simulations develop small, and sometimes multiple, separation bubbles. It does not appear that these

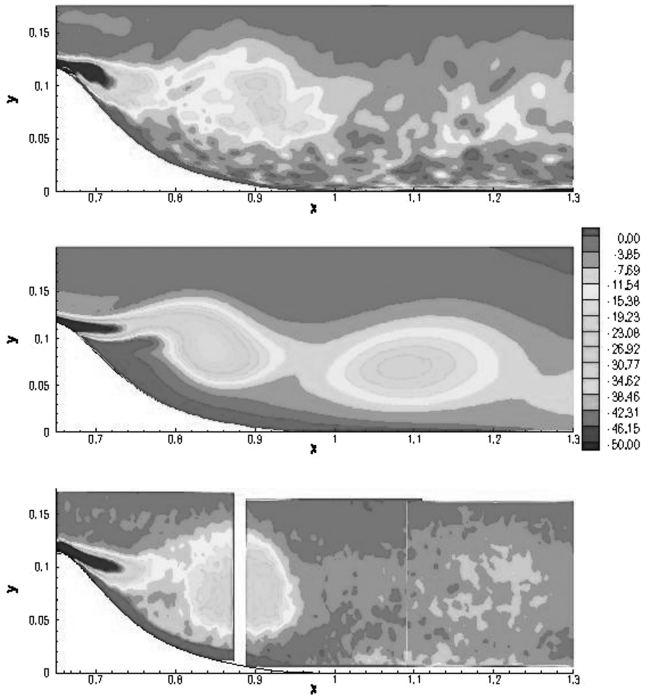

Fig. 27 Oscillating blowing-and-suction case: comparison between LA-OSC LES (top), RANS (middle), and Experimental PIV (bottom) phase-averaged z-vorticity contours at $\Theta = 90$ deg.

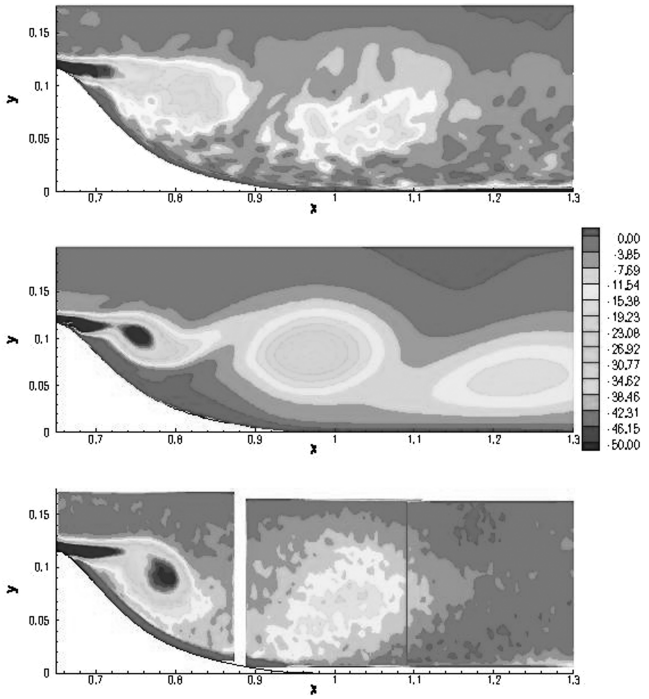

Fig. 29 Oscillating blowing-and-suction case: comparison between LA-OSC LES (top), RANS (middle), and experimental PIV (bottom) phase-averaged z-vorticity contours at $\Theta = 270$ deg.

recirculation regions existed in the experiment, but it is not clear because the experimental PIV data were considered unreliable within $y = 0.0012$ of the surface, due to wall reflections. This uncertainty also means that precise separation locations for the experiment are not available at each phase angle. A qualitative comparison between the numerical and experimental u-velocity contours suggests that separation in the LES and RANS solutions occurs somewhat upstream of the experiment at each phase angle. The Reynolds stress plots also display some general trends. The LES results seem to produce larger regions of higher magnitude $u'v'$ near the slot. The RANS simulations were on the other end of the spectrum, producing almost no Reynolds stress. This result seems to be consistent with what was observed in the time-averaged RANS solution shown in Fig. 23.

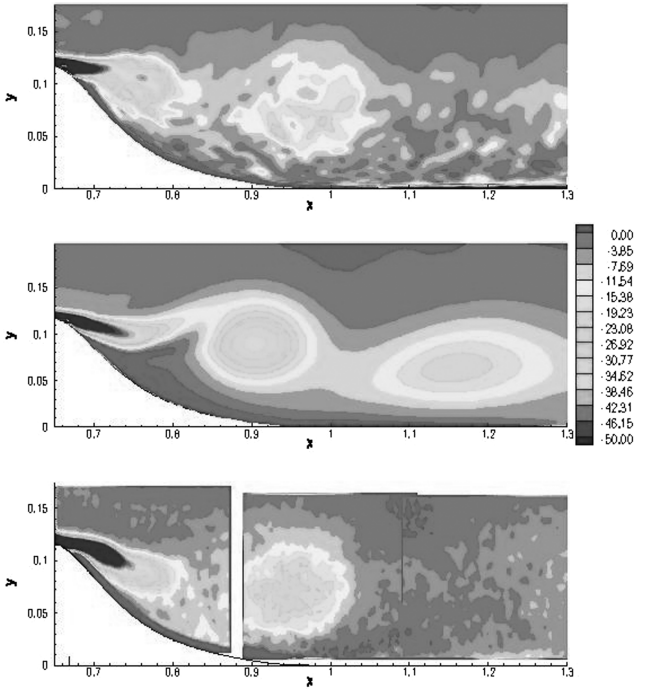

Fig. 28 Oscillating blowing-and-suction case; comparison between LA-OSC LES (top), RANS (middle), and experimental PIV (bottom) phase-averaged z-vorticity contours at $\Theta = 180$ deg.

VI. Conclusions

This work discussed the implicit LES of flow over a wall-mounted hump with and without flow control for the flow conditions of $M_\infty = 0.1$ and $Re_c = 2.0 \times 10^5$. Results from the flow control simulations were compared with the experiment and the baseline case with no flow control. The LES was conducted at a lower Reynolds number than the experimental value of $Re_c = 9.36 \times 10^5$ to maintain adequate LES-like resolution and to keep computational costs acceptable. Solutions were obtained using a 21-million-point mesh.

The current simulations demonstrated that the LES approach was capable of reproducing the correct qualitative character and magnitude of C_p for the baseline and flow control cases. All three cases displayed the correct physics in the recirculation region but did not perfectly match the experiment, because using a lower Reynolds number led to slightly longer separation bubbles. The LES predictions for the flow reattachment point downstream of the hump were within 4% of the experimental locations for the baseline and steady-suction cases. The oscillatory flow control case developed a reattachment location approximately 10% downstream of the experimental result. The reattachment location moved to within 2% of the experimental location by increasing the amplitude of the oscillating flow control by 250%. Overall, the LES predictions had behavior significantly closer to the experiment than previous RANS simulations for both types of flow control. Except for the velocity profile slightly upstream of the slot, which was very near the flow separation location, all other mean velocity, turbulent kinetic energy, and Reynolds stresses profiles and contour plots showed good agreement with the experimental data.

Based on the LES results of the baseline and flow control cases, it can be concluded that the implicit LES approach provides a significant improvement over RANS in modeling the separated flow region physics based on qualitative comparisons with experimental data. This result gives promise that when computer resources allow

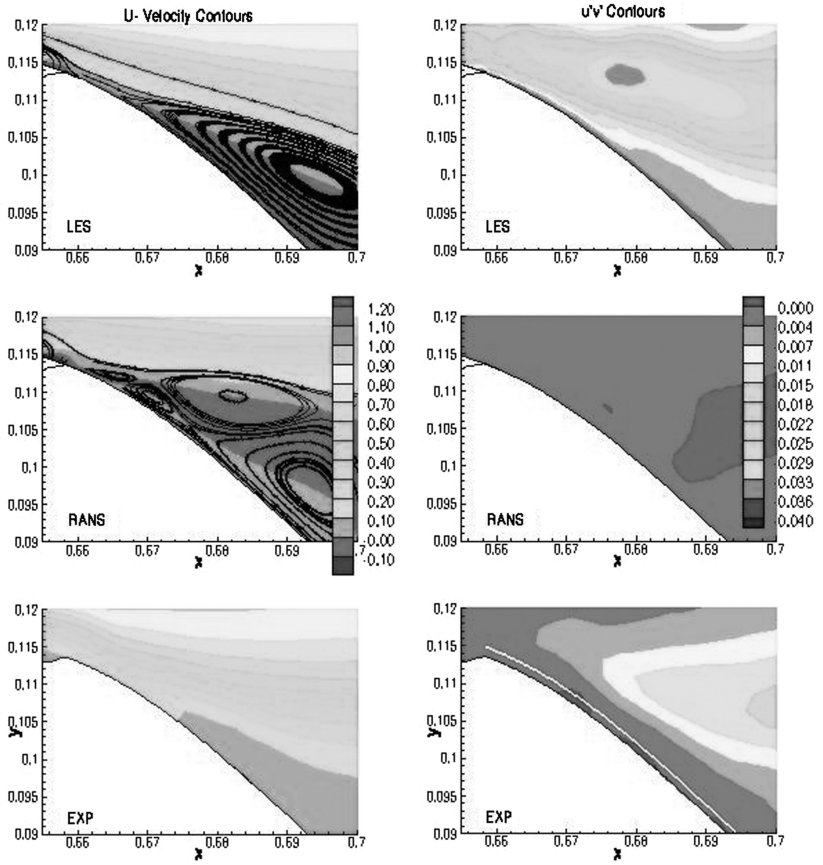

Fig. 30 Oscillating blowing-and-suction case: comparison between LA-OSC LES (top), RANS (middle), and experimental PIV (bottom) phase-averaged u-velocity and Reynolds stress contours near the slot at $\Theta = 0$ deg. (The area below the white line in the experiment indicates the region in which experimental PIV data are considered unreliable.)

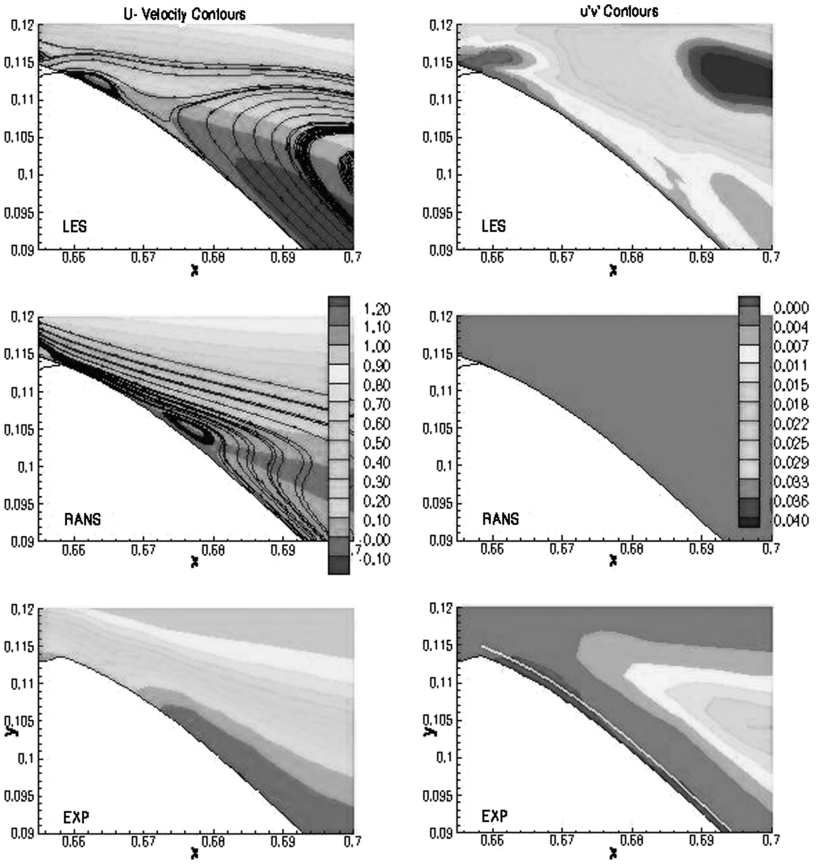

Fig. 31 Oscillating blowing-and-suction case: comparison between LA-OSC LES (top), RANS (middle), and experimental PIV (bottom) phase-averaged u-velocity and Reynolds stress contours near the slot at $\Theta = 90$ deg. (The area below the white line in the experiment indicates the region in which experimental PIV data are considered unreliable.)

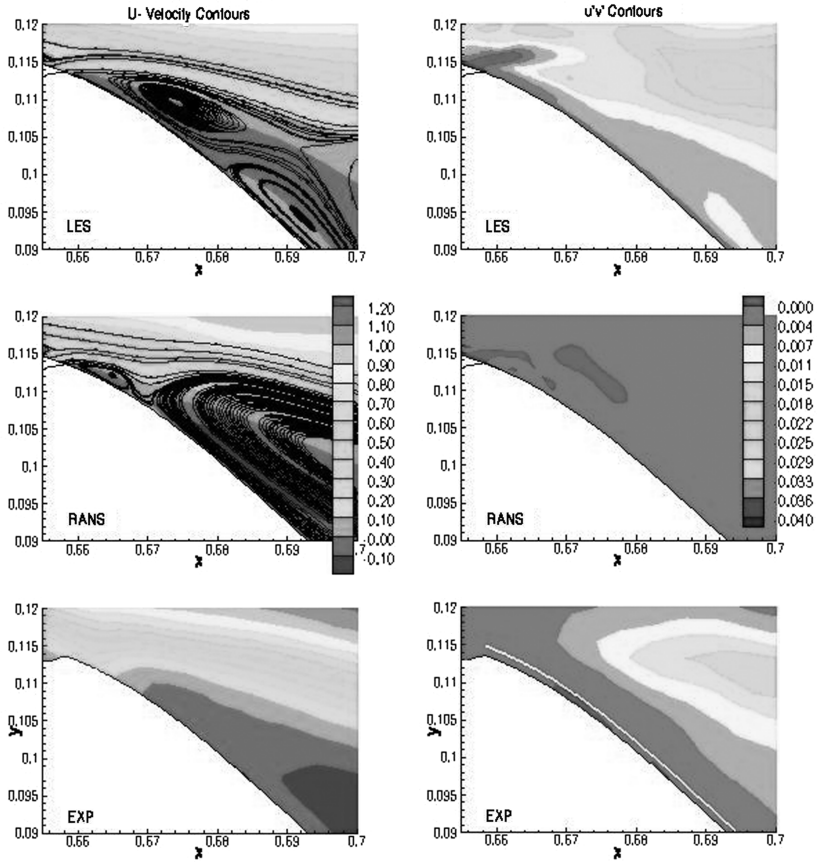

Fig. 32 Oscillating blowing-and-suction case: comparison between LA-OSC LES (top), RANS (middle), and experimental PIV (bottom) phase-averaged u-velocity and Reynolds stress contours near the slot at $\Theta = 180$ deg. (The area below the white line in the experiment indicates the region in which experimental PIV data are considered unreliable.)

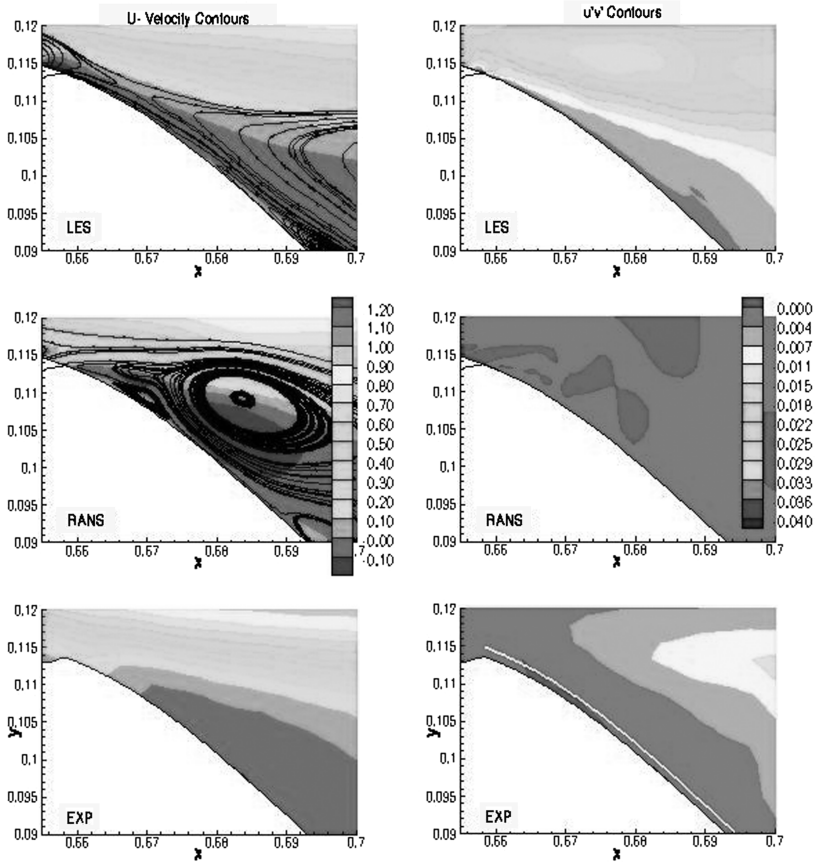

Fig. 33 Oscillating blowing-and-suction case: comparison between LA-OSC LES (top), RANS (middle), and experimental PIV (bottom) phase-averaged u-velocity and Reynolds stress contours near the slot at $\Theta = 270$ deg. (The area below the white line in the experiment indicates the region in which experimental PIV data are considered unreliable.)

for a LES at the full experimental Reynolds number, complete agreement with the experimental results might be achieved.

Acknowledgments

The authors are grateful for the U.S. Air Force Office of Scientific Research (AFOSR) sponsorship under a task monitored by T. Beutner. This work was also supported in part by grants of computer time from the U.S. Department of Defense Major Shared Resource Centers at Wright–Patterson Air Force Base, Ohio; at the John C. Stennis Space Center in Bay St. Louis, Missouri; and in Kihei, Hawaii.

References

[1] Seifert, A., and Pack, L., "Active Flow Separation Control on Wall-Mounted Hump at High Reynolds Numbers," *AIAA Journal*, Vol. 40, No. 7, July 2002, pp. 1363–1372.

[2] Rumsey, C., Gatski, T., Sellers, W., Vatsa, V., and Viken, S., "Summary of the 2004 CFD Validation Workshop on Synthetic Jets and Turbulent Separation Control," AIAA Paper 2004-2217, June 2004.

[3] Greenblatt, D., Paschal, K., Yao, C., Harris, J., Schaeffler, N., and Washburn, A., "A Separation Control CFD Validation Test Case, Part 1: Baseline and Steady Suction," AIAA Paper 2004-2220, June 2004.

[4] Greenblatt, D., Paschal, K., Yao, C., and Harris, J., "A Separation Control CFD Validation Test Case, Part 2: Zero Efflux Oscillatory Blowing," AIAA Paper 2005-0485, Jan. 2005.

[5] Seifert, A., and Pack, L., "Compressibility and Excitation Location Effects on High Reynolds Numbers Active Separation Control," *Journal of Aircraft*, Vol. 40, No. 1, Jan. 2003, pp. 110–119.

[6] Pack, L., and Seifert, A., "Dynamics of Active Separation Control at High Reynolds Numbers," AIAA Paper 2000-0409, Jan. 2000.

[7] Morgan, P., Rizzetta, D., and Visbal, M., "Numerical Investigation of Separation Control for Flow over a Wall-Mounted Hump," AIAA Paper 2004-2510, June 2004.

[8] Rizzetta, D., and Visbal, M., "Large-Eddy Simulation of Supersonic Cavity Flowfields Including Flow Control," *AIAA Journal*, Vol. 41, No. 8, Aug. 2003, pp. 1452–1462.

[9] Rizzetta, D., and Visbal, M., "Large-Eddy Simulation of Supersonic Compression-Ramp Flows by a High-Order Method," *AIAA Journal*, Vol. 39, No. 12, Dec. 2001, pp. 2283–2292.

[10] Rizzetta, D., and Visbal, M., "Application of Large-Eddy Simulation to Supersonic Compression Ramps," *AIAA Journal*, Vol. 40, No. 8, Aug. 2002, pp. 1574–1581.

[11] Morgan, P., Visbal, M., and Rizzetta, D., "A Parallel High-Order Flow Solver for Large- Eddy and Direct Numerical Simulation," AIAA Paper 2002-3123, June 2002.

[12] Morgan, P., and Visbal, M., "Large-Eddy Simulation of Airfoil Flows," AIAA Paper 2003-0777, Jan. 2003.

[13] Morgan, P., and Visbal, M., "Large-Eddy Simulation Modeling Issues for Flow Around Wing Sections," AIAA Paper 2003-4152, June 2003.

[14] Rizzetta, D., and Visbal, M., "Numerical Investigation of Transitional Flow Through a Low-Pressure Turbine Cascade," AIAA Paper 2003-3587, 2003.

[15] Rizzetta, D., and Visbal, M., "Numerical Simulation of Separation Control for a Highly-Loaded Low- Pressure Turbine," AIAA Paper 2004-2204, 2004.

[16] Erlebacher, G., Hussaini, M., Speziale, C., and Zang, T., "Toward the Large-Eddy Simulation of Compressible Turbulent Flows," *Journal of Fluid Mechanics*, Vol. 238, May 1992, pp. 155–185.

[17] Visbal, M., Morgan, P., and Rizzetta, D., "An Implicit LES Approach Based on High-Order Compact Differencing and Filtering Schemes," AIAA Paper 2003-4098, June 2003, p. 15.

[18] Beam, R., and Warming, R., "An Implicit Factored Scheme for the Compressible Navier–Stokes Equations," *AIAA Journal*, Vol. 16, No. 4, 1978, pp. 393–402.

[19] Gordnier, R., and Visbal, M., "Numerical Simulation of Delta-Wing Roll," AIAA Paper 93-0554, January 1993.

[20] Pulliam, T., and Chaussee, D., "A Diagonal Form of an Implicit Approximate-Factorization Algorithm," *Journal of Computational Physics*, Vol. 39, No. 2, 1981, pp. 347–363.

[21] Lele, S., "Compact Finite Difference Schemes with Spectral-like Resolution," *Journal of Computational Physics*, Vol. 103, No. 1, Nov. 1992, pp. 16–42.

[22] Gaitonde, D., and Visbal, M., "High-Order Schemes for Navier–Stokes Equations:Algorithm and Implementation into FDL3DI," U.S. Air Force Research Labs, TR AFRL-VA-WP-TR-1998-3060, 1998.

[23] Visbal, M., and Gaitonde, D., "High-Order Accurate Methods for Complex Unsteady Subsonic Flows," *AIAA Journal*, Vol. 37, No. 10, 1999, pp. 1231–1239.

[24] Visbal, M., and Rizzetta, D., "Large-Eddy Simulation on Curvilinear Grids Using Compact Differencing and Filtering Schemes," *Journal of Fluids Engineering*, Vol. 124, No. 4, Dec. 2002, pp. 836–847.

[25] Visbal, M., and Gaitonde, D., "Very High-Order Spatially Implicit Schemes for Computational Acoustics on Curvilinear Meshes," *Journal of Computational Acoustics*, Vol. 9, No. 4, 2001, pp. 1259–1286.

[26] Gridgen User Manual Vers. 15, Pointwise, Inc., Forth Worth, TX, 2003.

[27] Ghosal, S., "Mathematical and Physical Constraints on Large-Eddy Simulation of Turbulence," *AIAA Journal*, Vol. 37, No. 4, Apr. 1999, pp. 425–433.

[28] Morgan, P., Rizzetta, D., and Visbal, M., "Large-Eddy Simulation of Flow over a Wall-Mounted Hump," AIAA Paper 2005-0484, Jan. 2005.

R. So
Associate Editor